UCLouvain

École polytechnique de Louvain

Swimming eel-like robot

Design, implementation and validation of a SEA

Authors: **Devillez Louis, Poncelet Gilles**
Supervisor: **Ronsse Renaud**
Readers: **Chatelain Philippe, Dehez Bruno, Bernier Caroline**
Academic year 2020–2021
Master [120] in Electro-mechanical Engineering

Abstract

This master thesis presents the design and implementation of a series elastic actuator (SEA), a torque controlled actuator for an eel-like robot. The SEA has as main component clock springs (a highly deformable spring). It has been developed with fast prototyping tools. The dimensioning was based on the CFD simulation of the swimming eel robot controlled by a central pattern generator (CPG) law. The resulting SEA is compact and lightweight, making it easy to add to the actual floating robot. Furthermore, its static validation shows high linearity and bandwidth only limited by the motor.

This work also explores the control of this SEA with a middle-level controller for the torque in the joint and a high-level controller for the angular position. Two versions of this second controller were implemented: a pure feedback law and a feedforward with feedback law. The latter shows a very stable behaviour with low steady state error.

Keywords: Eel-like Robot, SEA, Multi-Body Systems, Compliance, Feedback, Feedforward, CPG

Acknowledgments

First and foremost, we have to thank our research supervisor, Pf. Ronsse Renaud. Without his assistance and dedicated involvement in this project, this master thesis would have never been accomplished. We would like to thank you very much for your support over this academic year.

We would also like to show our gratitude to Pf. Herman Benoît who gave us help and advice on the mechanical design, the 3D printing of the parts and for letting us use the MakingLab.

We would also like to thank Bernier Caroline for her supervision on the project and expertise, for her help on the simulator and for being a reader of this work.

We are also grateful to Pf. Chatelain Philippe for his advice concerning the project and for being a reader of this work.

We would also like to acknowledge Pf. Dehez Bruno as the third reader of this thesis.

We would also like to thank the technicians from "HALL LEFT" and more particularly Vervotte Julien for his technical advice and help concerning the experimental part of this project.

We would also like to thank Leduc Astrid and Hennau Isabelle for their time and reactivity when orders were placed.

Finally, we must express our very profound gratitude to our families and friends for their unfailing support and continuous encouragement during this project. This accomplishment would not have been possible without them.

Thank You,

Devillez Louis & Poncelet Gilles

Glossary

τ_{FB} Feedback torque contribution.

τ_{FF} Feedforward torque contribution.

θ_L Output angle of the SEA (load angle).

θ_M Output angle of the Dynamixel (motor angle).

θ_S Output of the SEA encoder, defined as the difference between the load and motor angles $\theta_M - \theta_L$.

$\hat{y}$ Reference value for the signal y.

y True value of the signal y.

y^* Error made on the signal y: $y^* = \hat{y} - y$.

CPG Central pattern generator.

SEA Series elastic acutator.

Contents

1 Introduction **7**
- 1.1 State of the art . . . 8
  - 1.1.1 Fish robot . . . 8
  - 1.1.2 Anguiliform robot . . . 10
- 1.2 State of the project and objectives . . . 13

2 Problem statement **17**

3 Design of a torque controlled actuator **22**
- 3.1 Design process . . . 22
  - 3.1.1 Current measurement . . . 23
  - 3.1.2 Electrical power method . . . 24
  - 3.1.3 Reaction torque measurement . . . 24
  - 3.1.4 Direct torque measurement . . . 25
  - 3.1.5 Series Elastic Actuator . . . 26
  - 3.1.6 Comparison and selection of solution . . . 26
- 3.2 Impact of the stiffness . . . 28
- 3.3 Design of the SEA . . . 31
  - 3.3.1 Design inspiration . . . 31
  - 3.3.2 Final design . . . 32
  - 3.3.3 Update of the transmission . . . 36

4 Control **38**
- 4.1 Low-level motor controller . . . 39
- 4.2 Middle-level torque controller . . . 40
- 4.3 High-level position controller . . . 40
- 4.4 Hardware & software implementation . . . 41
  - 4.4.1 Middle-level controller . . . 41
  - 4.4.2 High-level controller . . . 43
  - 4.4.3 Physical layout . . . 43

5 Validation **45**
5.1 SEA . . . 45
5.1.1 Static validation . . . 45
5.1.2 Dynamic validation . . . 47
5.2 Middle-level torque controller . . . 48
5.3 High-level position controller . . . 50
5.3.1 Feedback position controller . . . 50
5.4 Two-link system . . . 52
5.4.1 Feedback only . . . 52
5.4.2 Feedforward and feedback . . . 53

6 Conclusion **60**

A Colouring agent **62**

B Hardware **65**
B.1 Cost of the SEA . . . 65
B.2 Electronics . . . 65

Chapter 1

Introduction

Bio-mimicry is the emulation of nature with the purpose of solving complex problems. For example, fishes and other aquatic animals should be observed to improve our naval means of transport. Robotic fishes can also be used as scientific tools or find application in marine fields (inspection, rescue ...).

As seen in FIGURE1.1, there is a continuous variation between undulation and oscillation for this kind of swimming. The division into categories is made in function of the proportion of the body used for the propulsion. There are other kinds of swimming like Median and Paired Fin (MPF) locomotion.

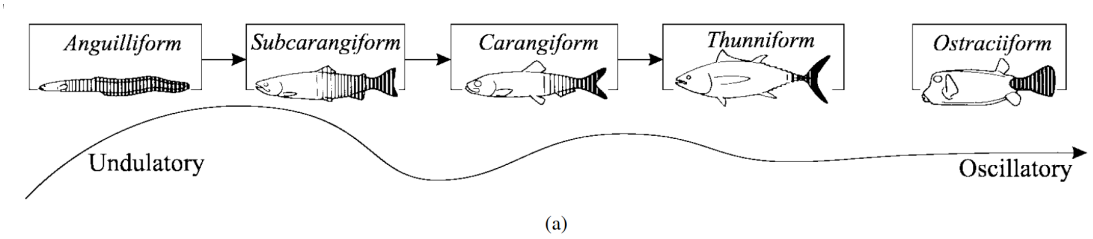


Figure 1.1: Swimming mode associated with a Body and/or Caudal Fin (BCF) propulsion. Adapted from [1].

In the present work, we discuss the design of an anguilliform like swimming robot. The rest of this chapter will present the state-of-the-art in terms of robotic fish. It will also present the current state of the eel-robot project developed at the UCLouvain, on which we are working. Chapter 2 will present the focus of the current work in line with the previous iterations. Then, chapter 3 presents the design process of a Series Elastic Actuator, which is then used to construct a torque-based controller for the eel-robot. The overall developed controller is detailed in chapter 4. Finally, we will present our experimental results and validations in chapter 5, followed by a conclusion in chapter 6.

1.1 State of the art

1.1.1 Fish robot

Ostraciiform

Ostraciiform body/caudal fish locomotion requires high-frequency oscillations of the caudal fin, yielding negligible body oscillations. It is the ideal form of bio-mimetic locomotion for underwater robots where body stabilisation is required for photography or manipulation applications [2].

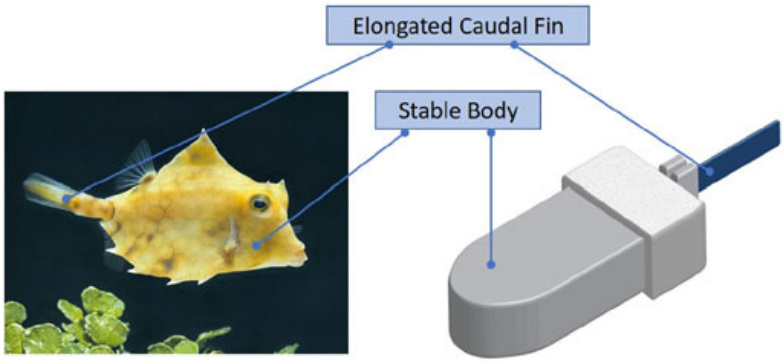


Figure 1.2: Ostraciidae fish (left), bio-mimetic ostraciiform underwater robot (right) [2].

In [2] the authors propose a robot with 2-segment caudal fin (FIGURE1.2) to improve the oscillation amplitude and have a wide-range frequency of oscillation.

Thunniform

In thunniform swimming, the body is not rigid anymore. This propulsion method has more propulsive efficiency than ostraciiform swimming. The most well known thunniform robot is the RoboTuna from MIT. The project was to evaluate the viability of a submarine reproducing the swimming of a tuna.

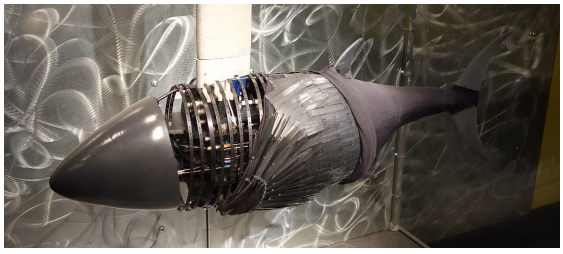


Figure 1.3: Robotuna on display at the MIT Museum [3].

In [4], the authors design a transmission mechanism (FIGURE1.4) with a single motor to achieve harmonic roto-translation. According to them, it has the highest propulsive efficiency in biological underwater locomotion.

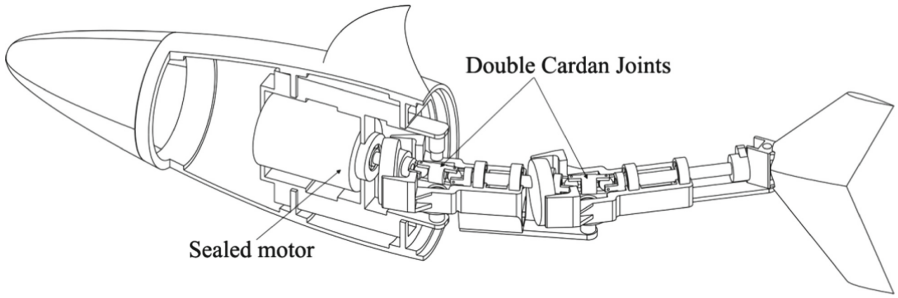


Figure 1.4: Assembly of the transmission system (tail and fin) and the thunniform robot fore-body [4].

Carangiform

In a carangiform fish (e.g. carp), the tail (third of the body length) can also undulate. Those fishes have better manoeuvring capabilities but are slower than thunniform. The university of Essex is designing a series of carangiform robot (FIGURE1.5). The project is at the 9th generation. The robot is able to accelerate, decelerate and take a sharp turn.

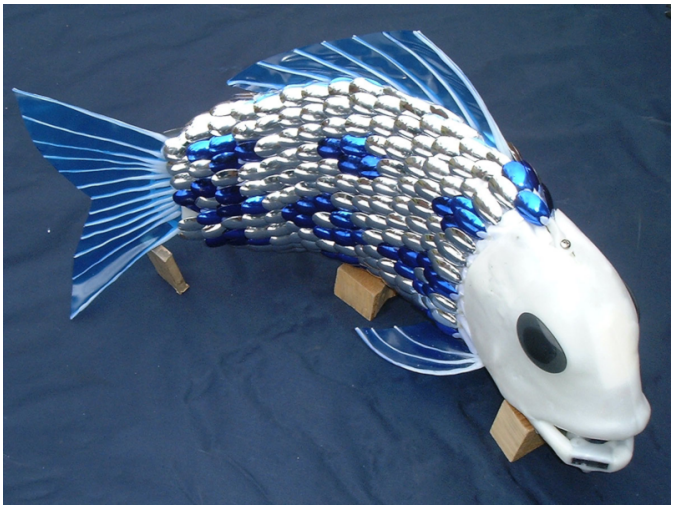


Figure 1.5: G6 Carangiform robot from Essex Robotics Research [5].

1.1.2 Anguiliform robot

Anguilliform robots are the most interesting ones for this project. Eels use the low-pressure regions generated by the undulation of their body in the fluid to propel themselves, achieving efficient swimming. Anguilliform swimming also provides a high degree of maneuvrability and the ability to swim backwards. Hereunder, a brief history of a non-exhastive list of those robots and their main characteristics is presented.

Northeastern University's Undulatory Underwater robot

First presented in 1999, it is one of the first anguiliform robot. Its design is based on a lamprey and it uses shape memory alloy actuators. This robot (FIGURE1.6) had no sensorial feedback but a CPG which decides to activate or not an actuator was implemented.



Figure 1.6: Lamprey robot developed by the the Northeastren University [6].

Robotic EEL

The REEL robot (FIGURE1.7) has been designed by McIsaac and James P. Ostrowski [7]. They proposed in 1999 a robot made of 4 segments actuated by servo-motors. The robot was radio-controlled and implemented the following CPG law:

$$\phi_i = A\sin(\omega t + (i-2)\phi_s) \tag{1.1}$$

Moreover, this robot presents modularity as sections can be added and removed at will.

Robot Anguille from ROBEA project

The purpose of the ROBEA project is to design, study and make an eel robot (FIGURE1.8) being able to swim in 3 dimensions [8]. The design is a series of parallels elements. This robot uses a skin to be waterproof. The following law was implemented to swim in a horizontal plane:



Figure 1.7: REEL II by Kenneth A. McIsaac and James P. Ostrowski [6].

$$K_3(t, X, s) = C_a(X, s) \sin\left(2\pi\left(\frac{X}{\lambda} + \frac{t}{T}\right)\right) \tag{1.2}$$

Other developments were made to regulate the speed in the horizontal plane and to modify the height of the robot.



Figure 1.8: Eel robot from the ROBEA project [8].

ACM-R5

The ACM-R5 is Japenese robot (FIGURE1.9) made of sections. The number of sections is variable and can be modified by the user. Each section has embedded electronics to adapt the cinematics of the robot. Each joint has 2 degrees of freedom (yaw and pitch). It is designed for search and rescue missions.

ANGuiliform robot with ELectrical Sense

ANGELS is a European project with the goal to build a prototype of an autonomous reconfigurable robotic eel (FIGURE1.10) with electrical sens [10]. Each module is independent and moves with its own propulsor. Those modules can assemble themselves in a chain and move due to undulation of the whole body.

Lampetra

The Lampetra project aims to find new solutions for high-performance artificial locomotion (fast-response, adaptability, reliability, energy efficiency, control...) on a lamprey bioinspired robot(FIGURE1.11) [11]. They used novel actuators:



Figure 1.9: Snake-like robot ACM-R5 from Hirose-Fukushima Robotics Lab [9].

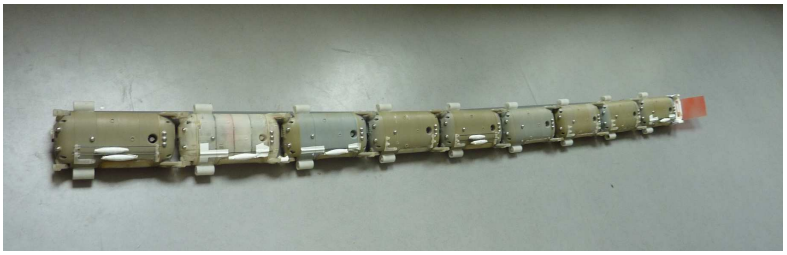


Figure 1.10: ANGELS robot with nine module [10].

permanent magnets rotated by servomotors. The actuator is force-controlled, back-drivable and allows stiffness adjustment. The robot is made of a high number of segments.



Figure 1.11: Robot made during the Lampetra project [12].

Amphibot I, II and III

Amphibot is an amphibious snake robot (FIGURE1.12). The project aims to build an amphibious robot for outdoor robotic tasks and to test adaptive controllers based on CPGs. It is composed of seven actuated elements and one head element.



Figure 1.12: Amphibot III from the EPFL [13].

Each actuated element contains a power board, a motor controller, a motor and a battery so that each element is independant (mechanically and electrically) [14]. The head element implements the CPG and sends out setpoints to the motor controllers of each element through I^2C. The implemented CPG law was the following:

$$\begin{cases} \dot{\theta}_i = 2\pi\nu_i + \sum_j r_j w_{ij} \sin\left(\theta_j - \theta_i - \phi_{ij}\right) \\ \ddot{r}_i = a_i \left(\frac{a_i}{4}(R_i - r_i) - \dot{r}_i\right) \\ x_i = r_i \left(1 + \cos(\theta_i)\right) \end{cases} \tag{1.3}$$

Pleurobot

Pleurobot is a salamander robot (FIGURE1.13) that can swim with an undulation movement and walk on the ground. This robot also embedded a CPG that control each of the servomotors.

1.2 State of the project and objectives

There are ongoing studies at UCLouvain about the efficiency of anguilliform swimming and the produced flow. During swimming, the eel uses the vortexes present in the water to improve its propulsion. This study helped create a theoretical model based on CFD (Computational Fluid Dynamics) simulations. In those simulations, the eel body is represented as a daisy chain of ellipses (FIGURE 1.14). BERNIER Caroline develops this simulator, and it will be referred to as CFD simulator later in this work.



Figure 1.13: Pleurobot robot from the EPFL [15].

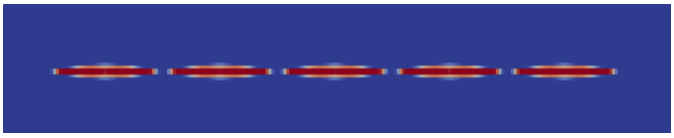


Figure 1.14: Representation of the eel robot (in red) in the CFD simulator.

The purpose of our project is to design an eel-like robot to make experimental comparisons with those simulations. The requirements of this robot were:

- The sections must have an ellipsoidal shape;
- The actuators and articulation must be above the water to prevent any interference with the flow;
- The robot should be able to move following a straight line (so the robot can be tested in LEFT Hall from Stévin building from UCL) with anguilliform swimming;
- The flow study must be done at half the height of the section to minimise undesired side effects;
- The articulation must be controlled in torque;
- Easy to add or remove an articulation;
- The robot must be stable in the water.

At the end of the first iteration [16], they successfully made an eel-like robot (Figure 1.15). It exhibited anguilliform swimming and could follow a straight line.

But its main drawback was the rolling stability in water. Work was done on the waterproofing. The sections were 3D printed with PLA but required some kind of assembly. Adding or removing section was also not so easy to do.

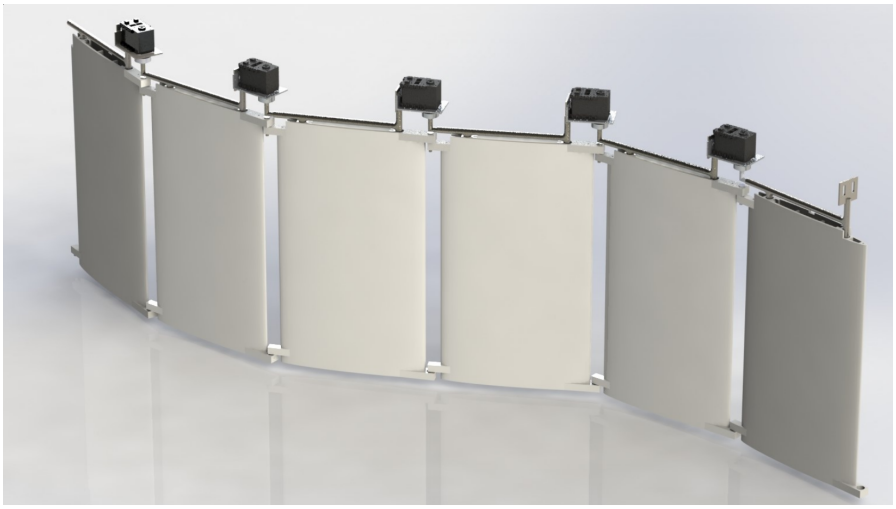


Figure 1.15: CAD representation of the eel-like robot at the end of the first iteration.

The second iteration [17] was focused on correcting this stability issue. They designed floats to add at the top of the section (Figure 1.16). They also closed the loop on the robot position using a camera detection system.

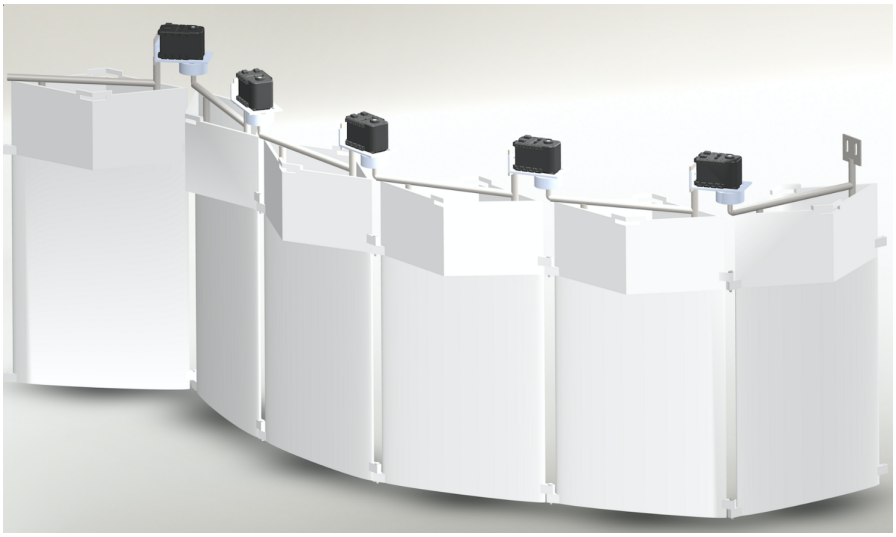


Figure 1.16: CAD representation of the eel-like robot at the end of the second iteration.

In this work, we will focus on making the robot joints torque-controllable. We have also advanced on the flow study, which will be covered in Appendix A

Chapter 2

Problem statement

The previous works on the eel-robot focused on position control of the robot joints. The studied control law was one of a descending sine wave of decreasing amplitude along the actuator chain, given by:

$$\hat{\theta}_{Li}(t) = A_i \sin(2\pi\nu t + \phi_i) \tag{2.1}$$

A CFD simulation of this law is shown in FIGURE 2.1.

In order to further attempt to accurately biomimicry the anguilliform swimming, this work will focus on the design and control of torque-controlled actuators for the eel-robot. The design process of such an actuator will be detailed in Chapter 3.

We also made the choice to work with another control law, based on the principle of central pattern generators (CPGs). The CPG law that will be used throughout this work is the one developed by the EPFL's Biorobotics Laboratory for their Amphibot robot [18, 19]. It is implemented as a network of coupled oscillators (FIGURE 2.2) and reads as follows:

$$\begin{cases} \dot{\theta}_i = 2\pi\nu_i + \sum_j r_j w_{ij} \sin\left(\theta_j - \theta_i - \phi_{ij}\right) \\ \ddot{r}_i = a_i \left(\frac{a_i}{4}(R_i - r_i) - \dot{r}_i\right) \\ x_i = r_i \left(1 + \cos(\theta_i)\right) \end{cases} \tag{2.2}$$

More specifically, we will focus on the asymptotic behaviour of this law, not on its transient phase. The limit cycle of the oscillators (2.2) is defined by the following for the i-th oscillator:

$$x_i(t) = \frac{A}{2}\left[1 + \cos\left(2\pi\nu t + i\Delta\phi + \phi_0\right)\right] \tag{2.3}$$

where ϕ_0 depends on the initial configuration of the system. The actuator position in the chain is defined as the difference between the corresponding left and right oscillators of the chain. Thus, the obtained asymptotic control law is

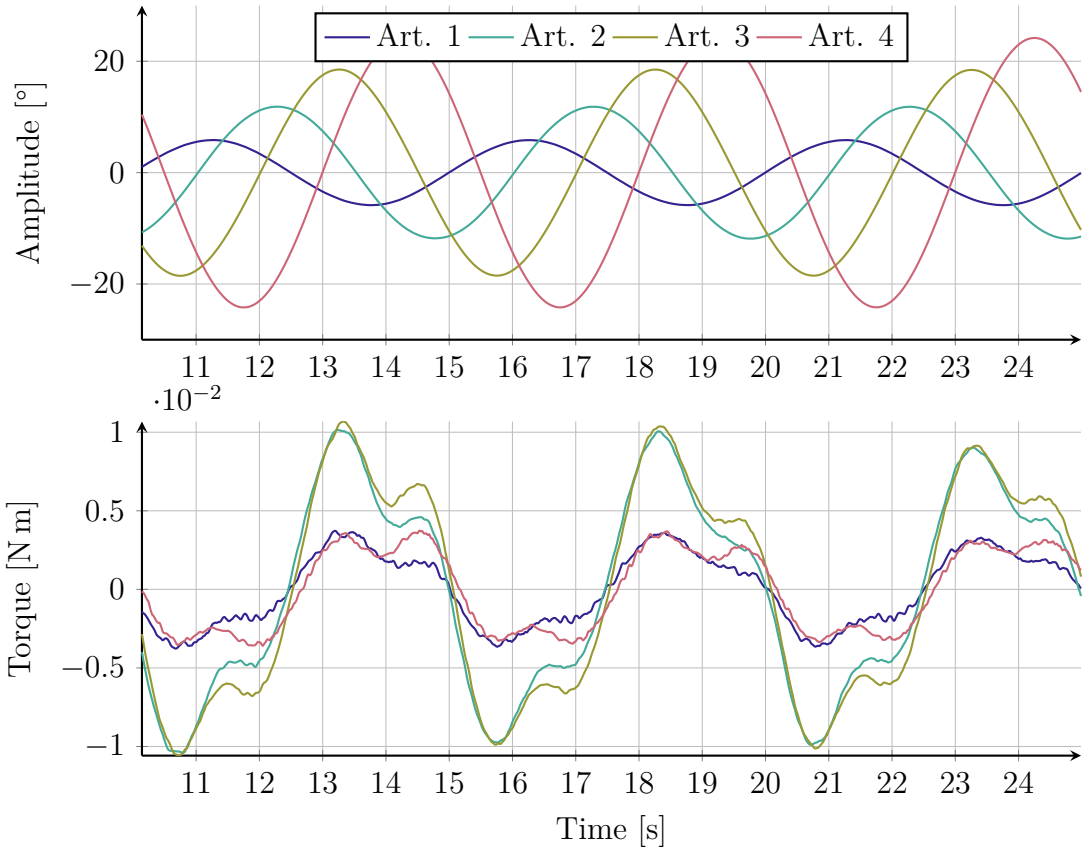


Figure 2.1: CFD simulation of the sine control law (2.1). Joint positions and torque are shown for five sections and four articulations.

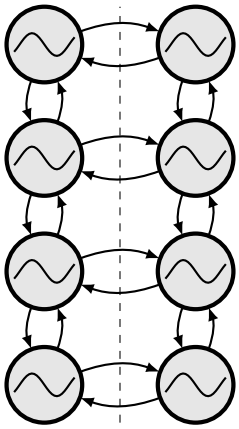


Figure 2.2: Schematic representation of the two chains of oscillators of a CPG.

that of a descending sine wave of constant amplitude (as opposed to the variable amplitude of the law (2.1)).

We choose the same parameters as for Amphibot, , i.e. $\nu_i = \nu = 0.2\,\text{Hz}$, $a_i = 100$, $\phi_{ij} = \pi$ for connections between left and right oscillators, $\phi_{ij} = \pm\Delta\phi = 1/N$ for ascending and descending connections and $R_i = A/2 = 15°$. The obtained result will serve as a reference for the rest of the work and is shown at FIGURE 2.3.

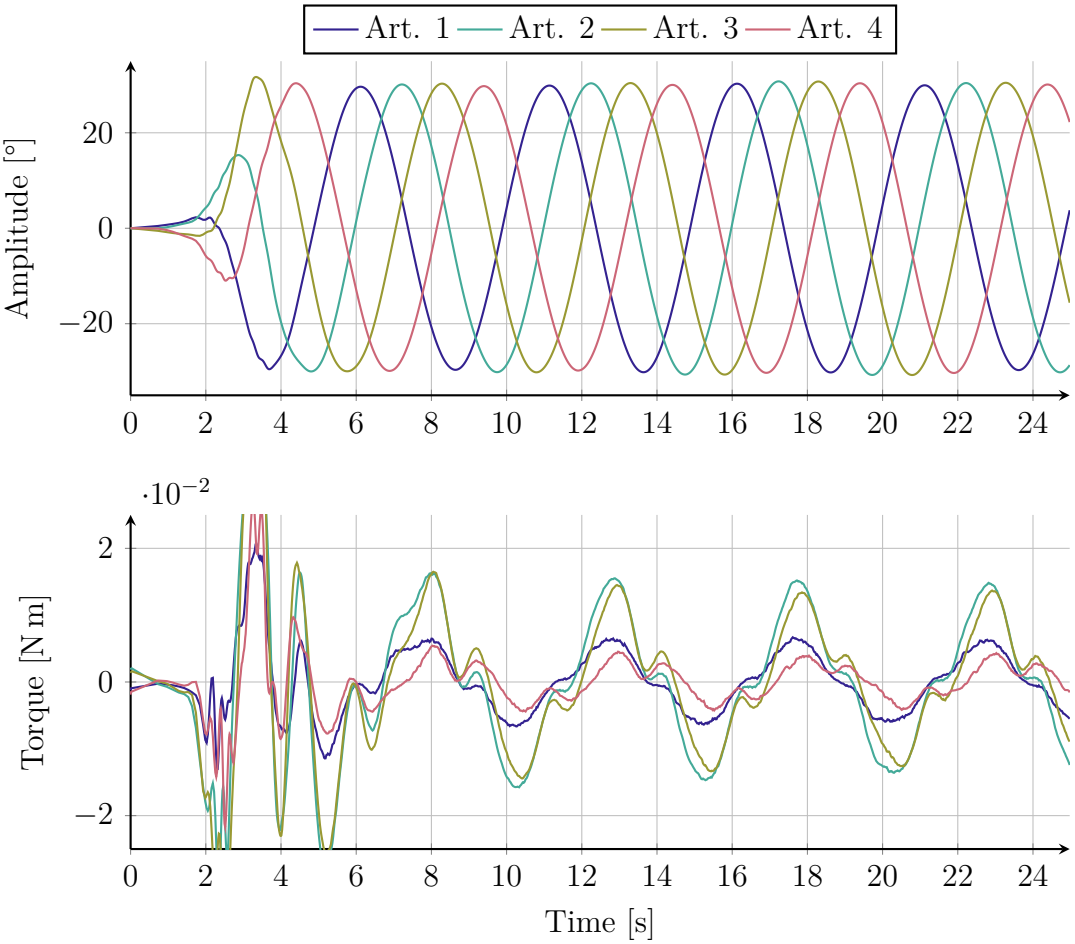


Figure 2.3: CFD simulation of the CPG control law. Joint positions and torque are shown for five sections and four articulations.

With the addition of torque-controlled actuators, it is no longer possible to directly impose a certain reference position. Instead, we need to have a reference torque. The same feedforward-based procedure could be used, and a design of some kind of reference torque law (CPG-based or even simpler) could be attempted. However, due to the ill-conditioned nature of the system, this will give rise to a fundamental stability issue. This instability is highlighted at FIGURE 2.4 where

we simulated a pure feedforward torque control law using the measured values generated by the CPG-based position control. Obviously, some sort of stabilization mechanism is required to stabilize the system. This can be achieved using two approaches:

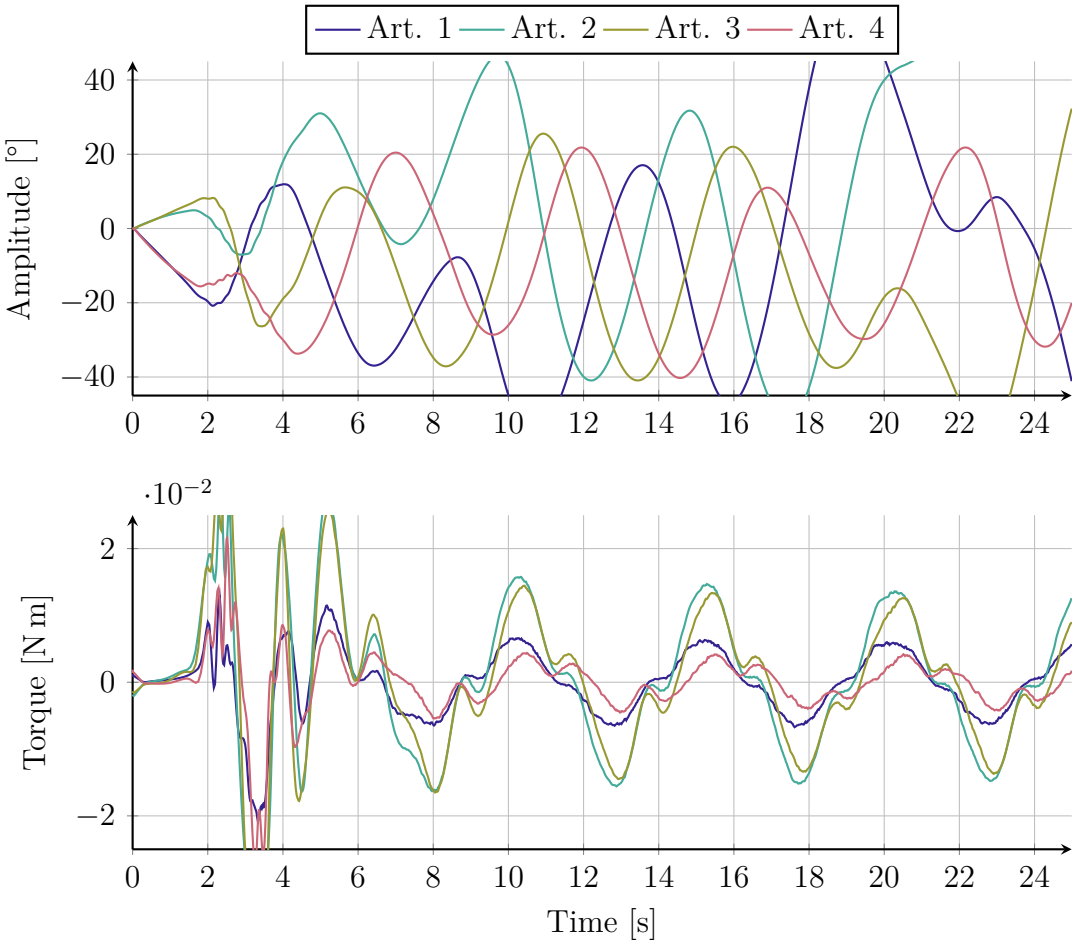


Figure 2.4: CFD simulation of a pure feedforward torque control law, following the torque generated by the CPG position control law. Joint positions and torque are shown for five sections and four articulations.

- Find which fundamental characteristic of a given feedforward torque control law (e.g. its frequency, amplitude, phase...) is most critical to the system stability and implement a feedback stabilization mechanism based on the selected parameter.
- Use a position-based feedback stabilization, using any given reference position (e.g. the CPG control law).

In this work, we chose to focus on the latter approach, as the former is likely more complex and could warrant its own research by itself. The details of the controller we developed to answer this question will be detailed in Chapter 4.

Chapter 3

Design of a torque controlled actuator

This chapter presents the design process behind our decision to design and implement a Series Elastic Actuator (SEA) in the eel-robot compared to alternative solutions. Then the constraints imposed by the system will be discussed. We will finish with the different features of our design.

3.1 Design process

The first step is to find the best-suited solution to answer our main goal: add a torque controlled actuator to the robot. At the end of iteration two, the robot was actuated by *Dynamixel AX12* which has a built-in load estimation but can not be used to accurately measure torque as stated on their website[1].

We started by comparing various possible solutions to measure torque. The following ones were found:

- Current measurement
- Electrical power meter
- Reaction torque measurement
- Direct torque measurement
- Series Elastic Actuators

[1] « Present load is an inferred value based on the internal output value; not a measured value using torque sensor.... Therefore, it may be inaccurate for measuring weight or torque. It is recommended to use it for predicting the direction and size of the force being applied to the joint. » [20]

3.1.1 Current measurement

The current measurement method (FIGURE 3.1) will measure the current flowing into the motor. By knowing some motor parameters, we can etablish the following equations:

$$\tau_{\text{em}} = k\phi I \tag{3.1}$$

$$\tau_{\text{out}} = \tau_{\text{em}} - \tau_p - J_t \frac{\partial \omega}{\partial t} \tag{3.2}$$

with:

- I the current flowing into the motor
- τ_{em} the electromagnetic torque
- $k\phi$ the motor torque constant
- J_t the momentum of inertia
- ω the motor speed
- τ_{out} the output torque
- τ_p the friction torque

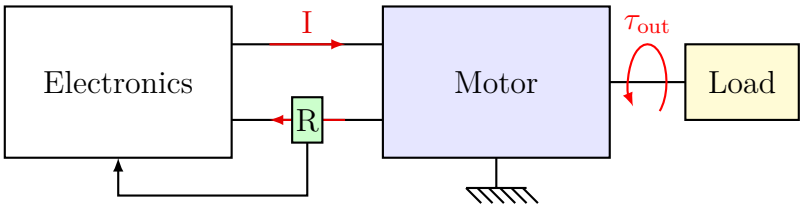


Figure 3.1: Scheme of current measurement to evaluate the torque.

This measurement will be done with a shunt resistor. The current flowing into the motor will also flow into this resistor which will cause a voltage drop through the resistor. This voltage can be then measured with a differential amplifier.

Thus, the motor's torque can be computed. However, the various losses (gearbox, coupling, friction...) should be accounted for as they can have a non-negligible impact on the output torque measurement. This measure can be further improved by factoring in the angular acceleration.

3.1.2 Electrical power method

This method is similar to the current measurement method. The tension applied to the motor is also measured with electronics, as well as the load speed (using an encoder), as depicted on FIGURE 3.2. With those value, the power can be computed as:

$$P_{\text{elec}} = U * I \tag{3.3}$$

$$P_{\text{out}} = \tau_{\text{out}} * \omega_{\text{out}} \tag{3.4}$$

$$\tau_{\text{out}} = \eta \frac{U * I}{\omega_{\text{out}}} \tag{3.5}$$

With:

- U the tension applied to the motor
- I the current flowing into the motor
- η the efficiency of the transmission
- ω_{out} the rotational speed of the output shaft
- τ_{out} the output torque

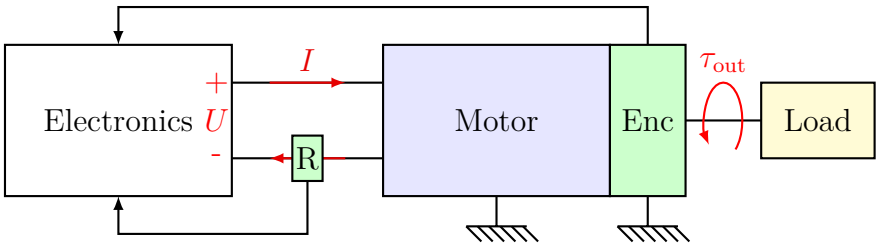


Figure 3.2: Scheme of the electrical power method to evaluate the torque.

The main drawback is the velocity measurement. We will not work at constant speed but with highly changing dynamics. Errors in the evaluation of ω_{out} will lead to high errors of τ_{out}. Here we have also the efficiency η to evaluate.

3.1.3 Reaction torque measurement

The reaction torque measurement uses Newton's third law. Instead of measuring the torque applied by the motor, the reactive torque applied by the motor on its

support is measured (FIGURE 3.3). This torque will induce deformation in the support, which are measurable with a strain gauge.

$$\frac{\Delta RL}{R\Delta L} = \frac{\Delta R}{R\epsilon} \tag{3.6}$$

With:

- ϵ the strain
- L original length
- ΔL absolute change in length
- R unstrained resistance of straing gauge
- ΔR change in strin gauge resistance
- τ_{out} the output torque

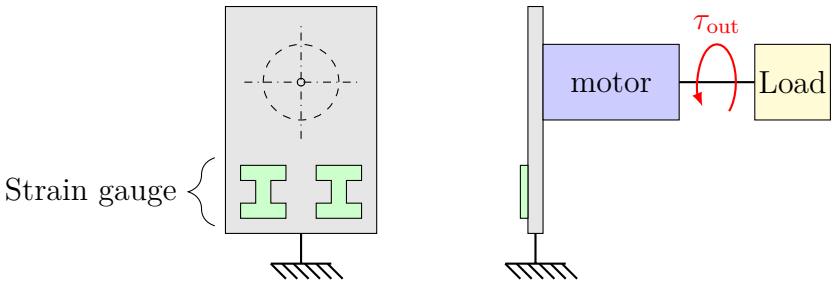


Figure 3.3: Scheme of reaction torque measurement.

By knowing the shape and properties of the material, the torque can be estimated. However, the measured torque here is also that of the motor and not of the articulation directly. Furthermore, the tolerance of the mechanical parts will also add uncertainties to the measurement.

3.1.4 Direct torque measurement

For the direct torque measurement, a sensor is placed between the motor and the load (FIGURE 3.4), and the shaft torsion is direcly measured using a strain gauge. As the load torque is directly measured, the transmission non-idealities do not need to be taken into account.

The main drawback is to have a rotating sensor, but as the rotation angle of the load is kept between $[-\pi, \pi]$, it is not a problem.

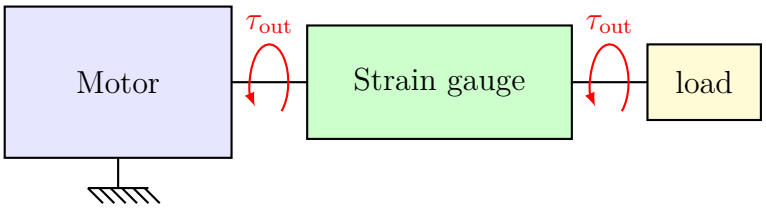


Figure 3.4: Scheme of direct torque measurement.

3.1.5 Series Elastic Actuator

The idea behind Series Elastic Actuator is close to the direct torque measurement. However, instead of using strain gauges to measure a microscopic deformation, we will use an elastic material between the motor output and the load (FIGURE 3.5), hence the name *series*. The macroscopic deformation of the elastic elements is measured and, knowing its material properties, the torque can easily be computed:

$$\tau_{\text{out}} = R * \Delta\theta \tag{3.7}$$

With:

- R: the stiffness of the elastic material in N m rad^{-1}
- $\Delta\theta$: the macroscopic deformation

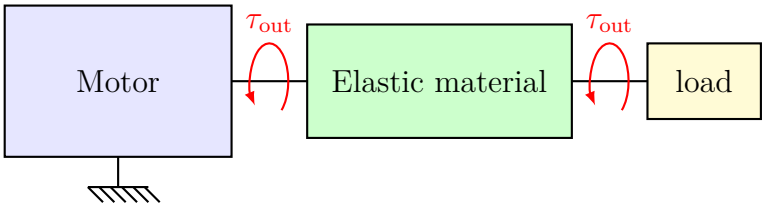


Figure 3.5: Scheme of a series elastic actuator to evaluate the torque.

To measure $\Delta\theta$, we can use two encoders (one for the motor and one for the load) or only one (the encoder is fixed with respect to the motor output and rotates with the load). Here, the load torque is also directly measured and the transmission effects can be ignored.

The SEA adds compliance to the articulation and also adds the possibility to exploit the resonance phenomenon of elastic elements to potentially save energy.

3.1.6 Comparison and selection of solution

We will now compare those solutions applied to our case. The following criterions are used:

- Price
- Weight: the robot should still be able to float
- Size: the robot should be able to accomodate the solution
- Precision: the robot should be controlled accurately, with a maximum torque of 0.4 N m (estimation obtained in the previous iterations of the project).

Criterion	- -	-	0	+	++
Weight [g]	$[200, \infty[$	[150,200[	[100,150[	[50,100[	$[0, 50[$
Size [cm^3]	$[800, \infty[$	[400,800[	[200,400[	[50,200[	$[0, 50[$
Precision [N mm]	$[16, \infty[$	[4, 16[	[1, 4[	[0.25 1[	]0, 0.25[
Price [€]	$[200, \infty[$	[150, 200[	[100, 150[	[50,100[	[0,50[

Table 3.1: Link between the quantitative criterion and a qualitative scale.

The result are in the TABLE 3.2 and the evaluation of those criterion in TABLE 3.1. We will now comment on those result:

- **Current measurement:** It is compact because it only needs some electronics to measure the current. The precision of the current measurement can be highly precise [21] (up to the ppm), but as the measurement is indirect, we prefer to take a safety factor. The shunt resistors are not costly (∼10 €), but the Dynamixel is a servomotor and not a motor, so we would also need to buy a motor and its gearbox.
- **Power measurement:** It has the same advantages and disadvantages as the current measurement. However, since it requires measurement of the speed, it will reduce the precision of the method.
- **Reaction torque measurement:** Only a few off-the-shelf sensors are made for our range of measurement. Even the low load transducer needs a minimal torque (∼0.1 N m [22]). To build a sensor, a strain gauge costs more than 60€ and it still requires precise tools to measure the resistance variation.
- **Direct torque measurement:** As the principle is the same for the reaction torque measurement, the results and conclusion are the same.
- **SEA:** This solution can be very precise by using a highly precise encoder or a low stiffness material. It will add weight to the robot (elastic material and its structure), but it can be kept relatively low by avoiding heavy metal pieces.

	Curr. Meas.	Pow. Meas.	Reac. Torq.	Dir. Torq.	SEA
Acc. & Prec.	0	- -	- -	- -	++
Size	++	++	+	+	0
Weight	++	++	++	++	+
Price	0	0	- -	- -	+
Total	4+ & 0-	4+ & 2-	3+ & 4-	3+ & 4-	4+ & 0-

Table 3.2: Comparison of solution to measure torque in our robot.

As we can see with the TABLE 3.2, the SEA and the current measurement are the best way to make a torque-controlled articulation for our robot and constrain. However, we chose to implement a SEA for the added compliance to the articulation (and the possibility to work at resonance frequency will also be studied).

3.2 Impact of the stiffness

To build a SEA, we need to choose an elastic material that will be defined by its rotational stiffness R or stiffness k. This spring is crucial for the design, and the SEA will be built around it.

The first step is to determine if we can profit from resonance phenomenon with an appropriate stiffness. For that purpose, we used the data from the simulator with the new law of control (FIGURE 2.3). The steady-state phase was isolated for both the position and the torque.

To analyse the impact of the spring we used the property that the torque is the same in each element of the transmission. We then compute the power consumption with an added spring element with stiffness R:

$$P_R = \tau \omega_R \tag{3.8}$$

$$\theta_R = \frac{\tau}{R} + \theta \tag{3.9}$$

With:

- P_R the power with a spring of stiffness R
- τ the torque
- ω_R the angular speed of the motor with a spring of stiffness R
- θ_R the position of the motor with a spring of stiffness R

- θ the position of the motor (and of the load) with no spring

From the results of FIGURE 3.6, it can be see that only the second articulation has a clear minimum at around $0.07\,\mathrm{N\,m\,rad^{-1}}$ (or $1.22\,\mathrm{N\,mm\,^{\circ -1}}$) for the average power. We can also see that the power will go up when the stiffness goes down, which is to be expected. The motor will have to move more to reach the same torque leading to a greater power consumption.

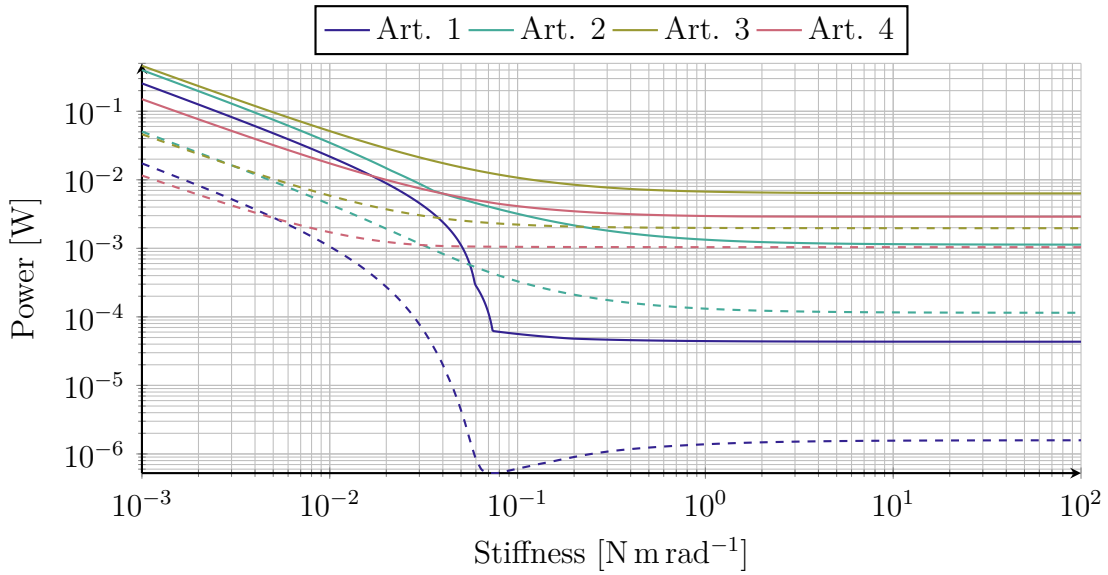


Figure 3.6: Max (plain line) and mean (dashed line) power computed with the data of the simulation with the CPG law of control for different stiffness of spring.

From this, we conclude that only the spring from articulation two will reduce power, but this reduction is directly linked to the dynamic of the robot. If we want to change the parameters of the control law, then the ideal stiffness changes as well. Furthermore, the total power is dominated by the power from articulation 3 and 4, making this power reduction minimal. So the best choice for our spring, with respect to the power, is to take the highest stiffness possible.

Another aspect to consider for the choice of spring is the resolution of the measurement. To measure the angular variation, we use an optical encoder which is limited to a number of ticks per revolution, so that it will define the resolution of measurement linked to a spring:

$$\Delta\tau = \frac{R * 2\pi}{n_{\text{ticks}}} \tag{3.10}$$

and we would like to reach a certain resolution linked to the maximum torque in the articulation,

$$\Delta\tau_{\text{SEA}} = \frac{\tau_{\max}}{2^{n_{\text{bit,res}}}} \tag{3.11}$$

By combining the two equations, we obtain:

$$R_{\text{opt}} = \frac{\tau_{\max} n_{\text{ticks}}}{2^{n_{\text{bit,res}}} 2\pi} \tag{3.12}$$

From this formula we can also extract $\Delta\theta$:

$$\Delta\theta_{\max} = \frac{2\pi 2^{n_{\text{bit,res}}}}{n_{\text{ticks}}} \tag{3.13}$$

The encoder we use have a resolution of 2048 ticks per revolution. However, using smart programming, this can be increased up to 8192 ticks per revolution. Using the same data as before, the power consumption ratio for a given measurement resolution can be estimated (FIGURE 3.7). The power ratio is computed as the following:

$$\nu = \frac{\sum_i P_{\text{R},i}}{\sum_i P_{\text{rigid},i}} \tag{3.14}$$

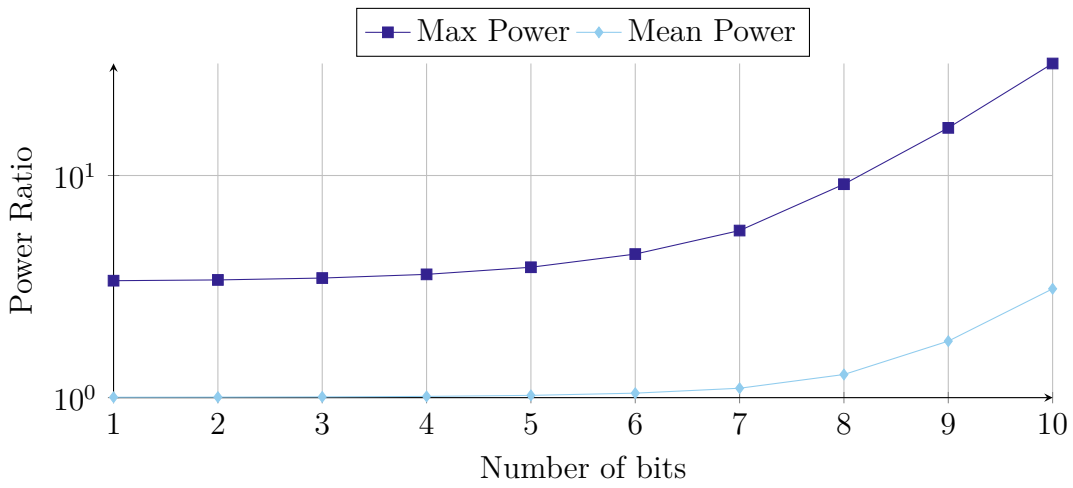


Figure 3.7: Power ratio of the SEA for different resolution for the torque measurement.

We chose to use the sum of the power because we use the same resolution for each articulation. With those results, we can now choose a number of bits for our precision and see the impact on the power. We choose $n_{\text{bit}} = 8$ which leads to an increase of the mean power by 27 %. The optimal stiffness for each articulation is in TABLE 3.3. This choice will also induce a minimum deformation of 11.25° that each SEA must be able to withstand.

	Art. 1	Art. 2	Art. 3	Art. 4
Stiffness [N m rad^{-1}]	0.034	0.080	0.074	0.023
Stiffness [N mm $^{\circ -1}$]	0.599	1.405	1.295	0.404

Table 3.3: Optimal stiffness for the spring material of the SEA to reach a resolution of 8 bits.

3.3 Design of the SEA

3.3.1 Design inspiration

The initial step was to look at other SEA designs. The first design (FIGURE 3.8) is based on compression springs but with a delocalized motor. The main advantage of this design is to have a high deformation angle (up to 90°). However, this design is quite bulky for our case. Furthermore, it will require a lot of changes to the actual robot.

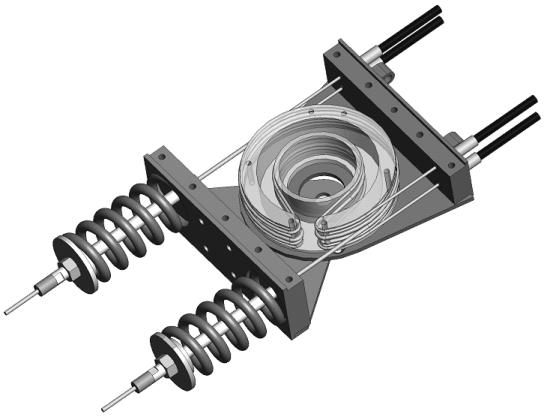


Figure 3.8: SEA design based on compression springs and bowden cable from [23].

The next design is more compact (FIGURE 3.9). It is based on several compression springs. It might fit our angular range, but the main drawback is the friction of the spring with their housing, thus inducing non-linearities in the torque measurement.

The third kind of design will eliminate the springs and use a single monolithic component (FIGURE 3.10). It is really compact, and the stiffness can be adapted (based on a FEM analysis), but the maximum deflection is too low for our application.

Those three designs are not suited for our application. It shows that we need to come up with an new design to fit within our constraints.

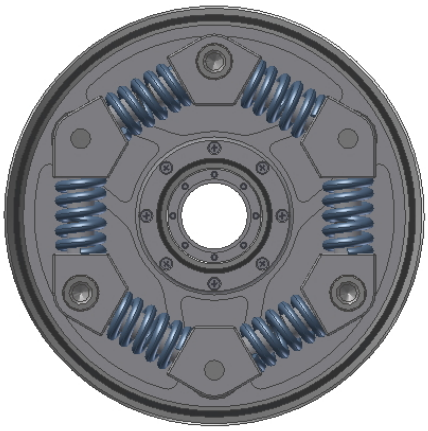


Figure 3.9: SEA design based on compression spring in a circular housing with a deflection of 5° from [24].



Figure 3.10: Monolithic SEA design based on FEM optimisation from [25].

3.3.2 Final design

As stated before, we want a SEA with the following properties:

- Lightweight
- High deflection (at the very least 11.25°)
- Compact
- Low effort of integration into the actual robot

We came up with a new design (Figure 3.11 and 3.12) composed of the following main parts (Figure 3.13):

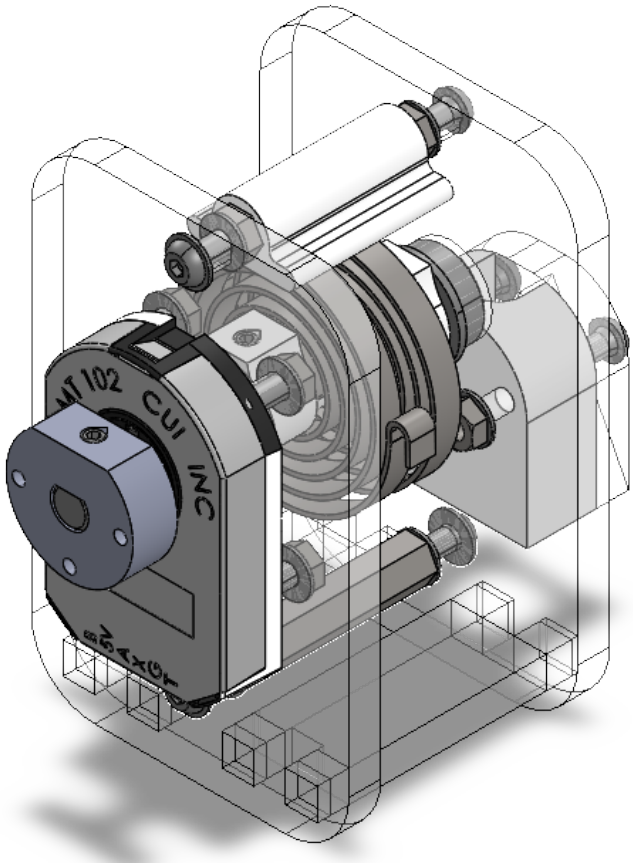


Figure 3.11: View of the CAD assembly of the SEA.

1. D-cut shaft
2. Adapter for the *Dynamixel AX12*
3. Encoder
4. Clock Springs
5. Spring support for the shaft
6. Ball bearing
7. Crosspiece
8. Spring support for the crosspiece
9. Rigidifier piece

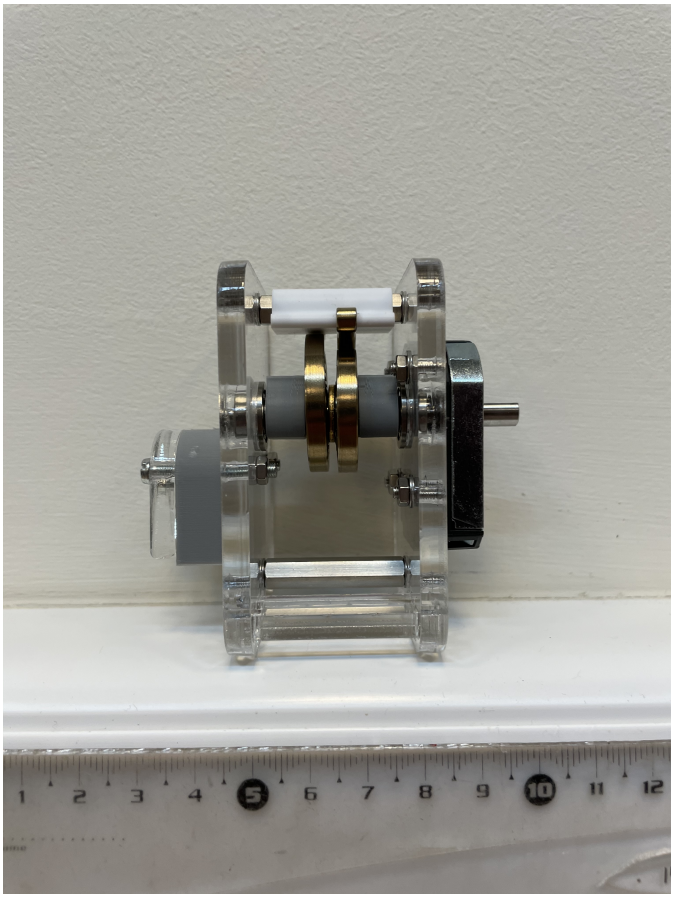


Figure 3.12: Picture of the final SEA with a ruler for a length comparison.

10. Output adapter
11. Output plate
12. Input structural piece
13. Output structural piece

The SEA works in the following way: the Dynamixel transmits its power to the shaft (1) through the adapter (2) that will rotate. This rotation compresses one spring (4) and uncompresses the other one (each spring is pre-compressed of 90°) through the spring support (5). The springs are mounted in opposite directions, so it will increase or decrease the torque. Finally, this torque is applied to another support (8) which will transmit the torque to the output (10) of the SEA through the crosspiece (7) and the output structural piece (13).

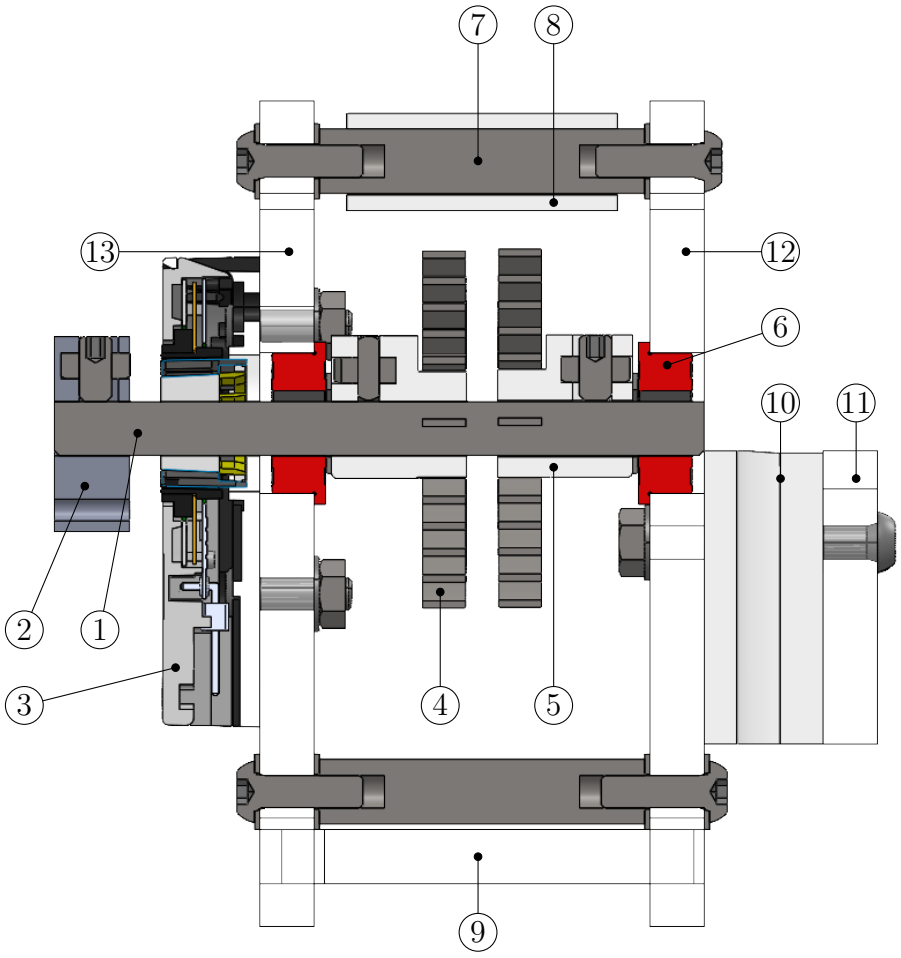


Figure 3.13: Sectional view of the CAD assembly of the SEA.

The D-cut shaft was chosen to add modularity to the design and move some of its elements with the help of socket screws. The 3D printed adapter was designed to follow this D-cut and have better transmission of the torque. We added two pieces (9) to rigidify the input and output (12 and 13). For the spring (4), we used clock springs because of their low width, the perfect range of stiffness and the high deflection range (up to 354°). The selected spring stiffness can be found in the TABLE 3.4 for each articulation. It must be noted that we have two springs in parallel, so the total stiffness of the articulation is twice the stiffness of a single spring. The design only requires 3D printing (PLA), laser cutting (acrylic glass), and off-the-shelf components.

To conclude on this section, the SEA indeed respects our constrains:

	Art. 1	Art. 2	Art. 3	Art. 4
Stiffness [N m rad^{-1}]	0.025	0.082	0.082	0.025
Stiffness [N mm °$^{-1}$]	0.43	1.43	1.43	0.43

Table 3.4: Spring stiffness in the SEA for each articulation.

- Lightweight: 120 g
- Compact: 76 mm X 70 mm X 50 mm
- Cheap: 98 €(the price of components can be found in TABLE B.1)

The main drawback is that some work is necessary to prepare the springs for the SEA (the D-cut shaft is too large for the springs). Also, the diameter could be reduced (and the weight), but it needs a D-cut along the whole shaft, and we did not find a cheaper option than a 6 mm shaft. Also, this design was made to allow modularity and, by knowing the final stiffness of the spring, we could reduce the length of the SEA. Another aspect that was not addressed in this work is the watertightness of the SEA (even if all the off the shelf components are in stainless steel to avoid degradation over time).

3.3.3 Update of the transmission

The SEA takes more space than the previous articulation, and the transmission needed to be adjusted. In the previous iterations, it was a structure of metal tube welded together, an L bracket to attach the Dynamixel, an adapter and a bent metal rod to transmit the torque to the next section. As the axis of rotation of the SEA must be aligned with the articulation of the two sections, we had to redo the metal structure. We also changed the L bracket to a laser-cut piece with a collar to simplify the assembly. Finally, the metal rod was replaced by the adapter already shown on the SEA. The evolution of the transmission can be seen in FIGURE 3.14 with the followings components:

1. *Dynamixel AX12* (actuator of the articulation)
2. Aluminium metal bracket
3. Off-the-shelf hub
4. Bended metal rod
5. Shaft collar
6. Metal tube

A comparison of the properties of the new section is shown in Table 3.5. The position of the centre of mass is expressed with the reference frame being at the bottom centre of the section. As we can see, the SEA adds a bit of weight ∼100 g and moves the height of the centre of mass only by ∼25 mm. We will need to remove some of the ballast to adjust the weight for the buoyancy, but it is still less than the weight limit, stated in the work of iteration 2, of 633 g.

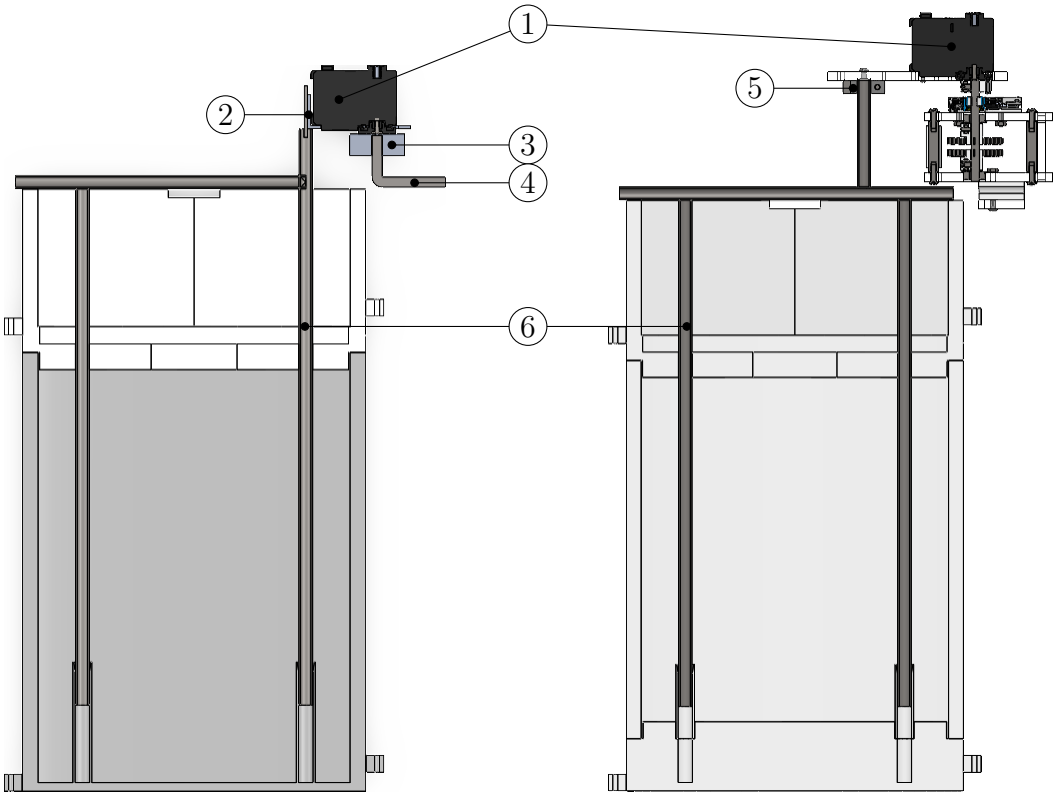


Figure 3.14: Sectional view of the CAD model of the old transmission (left) and the new one (right) with the list of main components.

	Mass [kg]	C_X [mm]	C_Y [mm]	C_Z [mm]
Old transmission	0.98	0	11.52	209.78
New transmission	1.07	0.24	21.55	233.26

Table 3.5: Comparision of the weight and dimensions between the old and new transmission.

Chapter 4

Control

This chapter discusses the implementation of the controller for the SEA. It will cover the conceptual implementation as well as the hardware/software implementation.

In practice, the controller is subdivided into three parts:

- A low-level motor controller (which is a black box in the context of our work so we will not modify its parameter)
- A middle-level torque controller
- A high-level position controller

An overall block diagram of the controller is given at FIGURE 4.1.

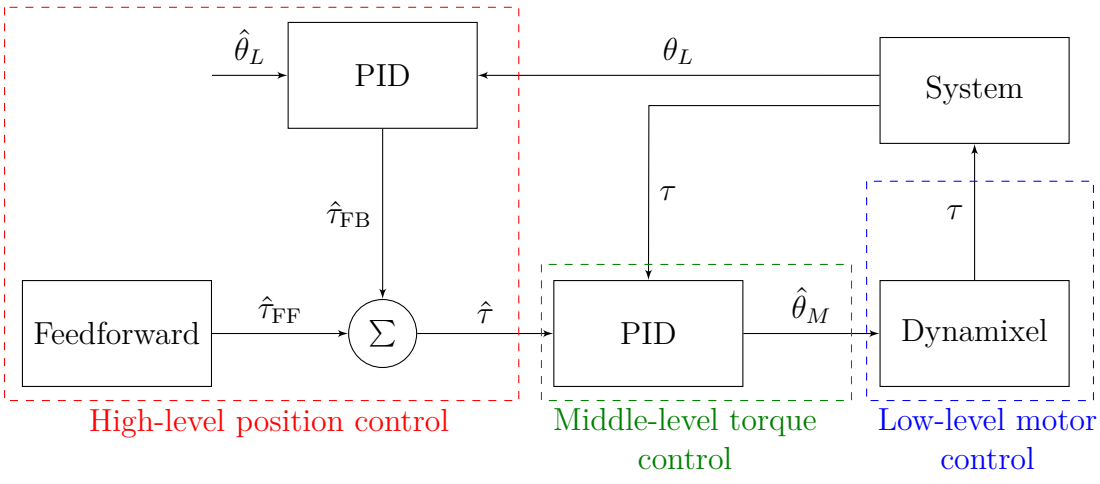


Figure 4.1: General block diagram of the SEA controller.

The follwing notation will be used to describe the different control variables:

- θ_L is the angular position of the physical articulation (SEA output)
- θ_M is the angular position of the Dynamixel (SEA input)
- θ_S is the angular position measured by the encoders

The relation between those 3 values is:

$$\theta_S = \theta_M - \theta_L \tag{4.1}$$

4.1 Low-level motor controller

The controller implemented can be found in the datasheet of the *Dynamixel AX12* [20]. Its purpose is to control the angular position of the motor, θ_M given a certain reference. It is implemented as a compliance controller (as shown on FIGURE 4.2) with 4 parameters:

- E: the punch
- K_m: the compliance margin
- K_s: the compliance slope
- $\tau_{\max}$: the maximum torque

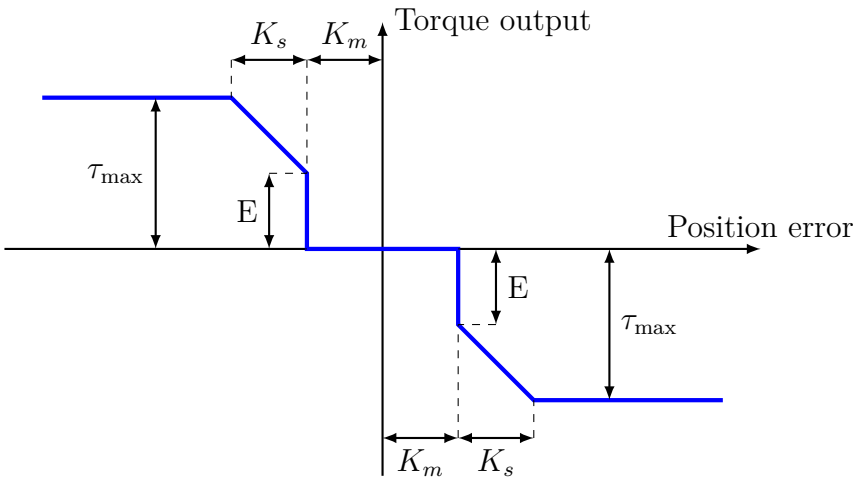


Figure 4.2: Schematic of the low-level controller implemented on the Dynamixel.

Those parameters can be manually changed on the Dynamixel. However, the default values work well enough that we do not need to change them. Furthermore,

we will consider the low-level controller's dynamic to be ideal (i.e. its response time is much faster than that of the middle-level controller), and it will be used in a black-box way.

More details about the Dynamixel protocol and hardware implementation can be found in [20].

4.2 Middle-level torque controller

The middle-level controller (FIGURE 4.3) controls the torque in the articulation, which is directly proportional to the SEA position θ_S and is computed as $\tau = R\theta_S$. It is implemented as a classical PID controller.

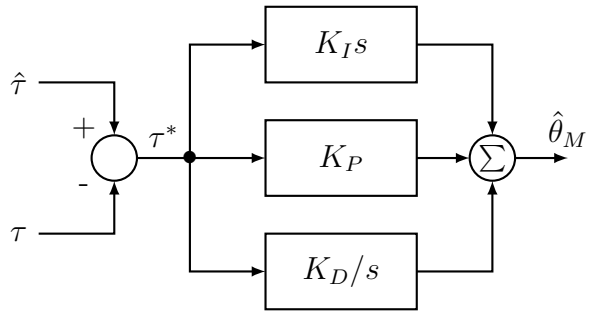


Figure 4.3: Schematic of the middle-level torque controller implemented on the Teensy.

4.3 High-level position controller

The high-level controllers drives the joint position θ_L. It has two contributions, shown on FIGURE 4.4:

- Feedback PID controller, in blue: its contributions τ_{FB} allows to stabilise the position around the tracking reference.
- Feedforward, in red: ideally, $\tau_{FF} = \hat{\tau}$. However in practice, this block is implemented as a simple approximation of the joint torque.

The feedforward contribution to the controller can be set to zero if no suitable approximation of the torque can be found a priori, but this generally degrades the controller's performance.

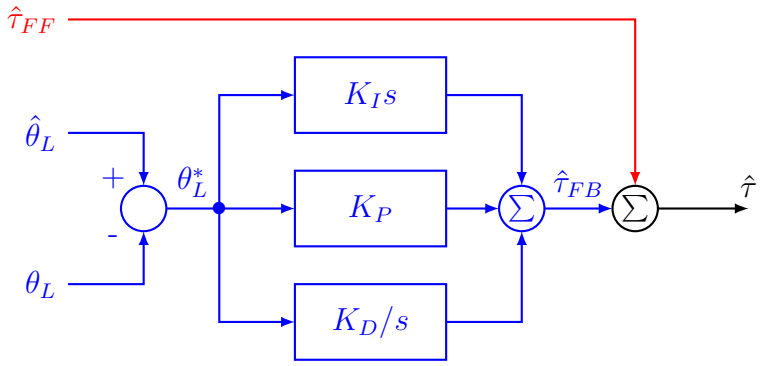


Figure 4.4: Schematic of the high-level position controller implemented on the computer. The feedback part is shown in blue and the feedforward is shown in red.

4.4 Hardware & software implementation

The previous iterations used an Arduino Micro MCU to control the daisy chain of Dynamixels. It was placed offboard, and three wires were used to communicate between the microcontroller and the robot.

However, with the SEAs, additional cabling is required to handle each encoder. To do so, we had to change the overall electronics of the eel-robot. We opted for a Teensy 4.1 microcontroller [26] for the following reasons:

- 600 MHz clock frequency: we wanted to implement the middle-level torque controller onboard, so a fast MCU was required.
- 55 I/0: we need more inputs for handling each encoder.
- 8 serial ports: those are required for the communication with the Dynamixel.
- 3 CAN ports: to prevent tedious cabling management, we placed the MCU onboard and opted for CAN communication between the MCU and the offboard computer due to its high robustness over long distances.

The main drawback of the Teensy is that it is not 5 V tolerant. To overcome this, we made a PCB to handle some electronics (Figure B.1).

4.4.1 Middle-level controller

The middle-level torque controller is implemented on the MCU, but its frequency is limited by the response time of the Dynamixel. In its basic configuration, after receiving a message (ping, instruction or request), the Dynamixel waits a certain

amount of time before responding. This delay can be reduced, but only up to 600 µs between each request.

This poses a significant bottleneck to the frequency of operations of the middle-level controller as it goes from 800 Hz for one articulation to 200 Hz for four articulations.

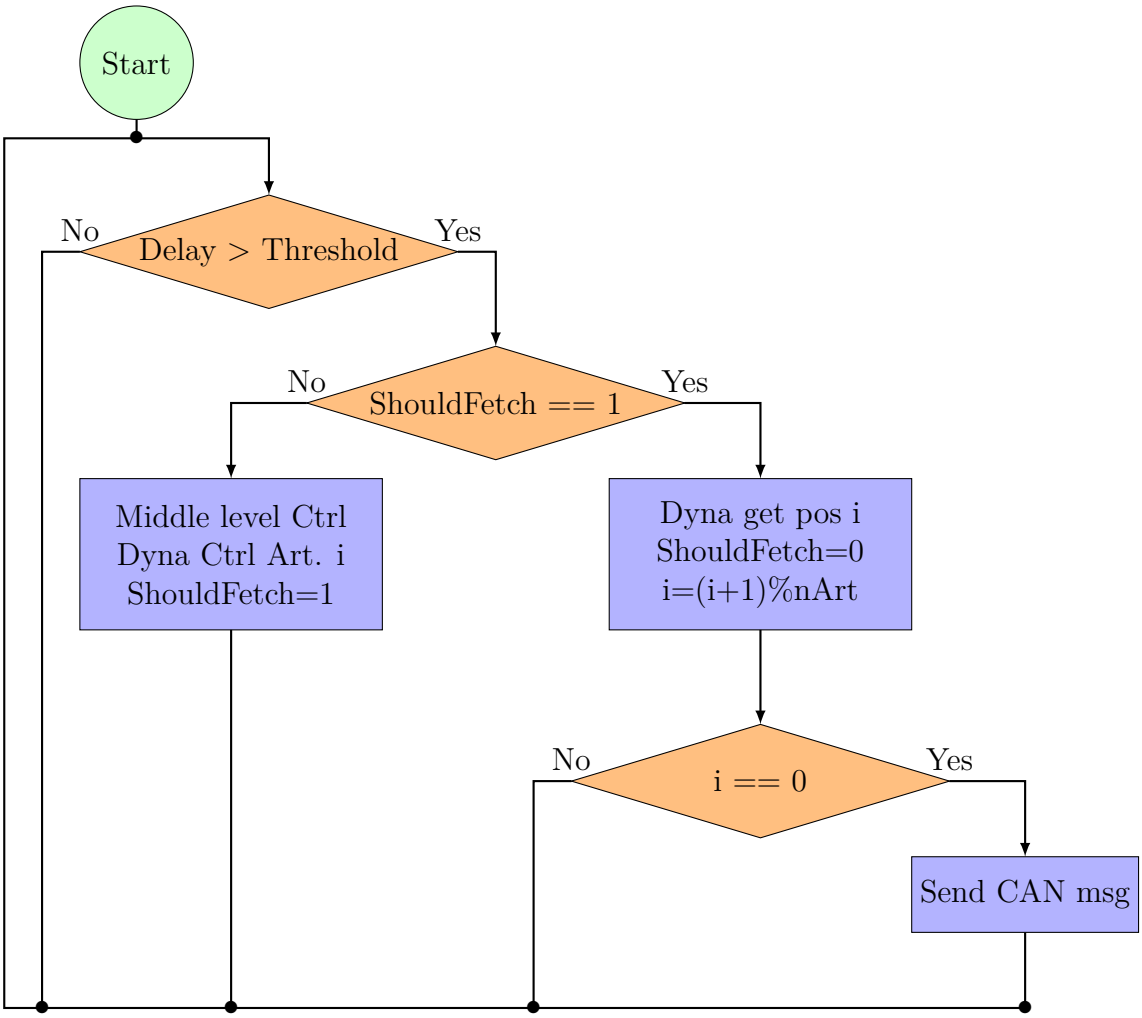


Figure 4.5: Flowchart of the middle-level controller implemented the Teensy.

This operational frequency is also the frequency at which CAN messages are broadcast over the CAN bus. A flow diagram of this part of the control is depicted in FIGURE 4.5. It shows the alternation between sending an instruction to the ith Dynamixel and getting its angular position. As the Dynamixels are daisy-chained, this operation is done on each articulation one after the other resulting in the varying control frequency. The Teensy also handles the reading of encoder values

using interrupts which are not shown on the diagram.

4.4.2 High-level controller

The high-level position controller was implemented on an offboard laptop in `Python`. As stated previously, the communication between the computer and the MCU is handled using a CAN bus. The main loop of the controller runs at approximately 100 Hz. A flow chart diagram of the program handling this part of the control is depicted in FIGURE 4.6. The computer also handles data logging and real-time visualisation (which are not shown on the diagram).

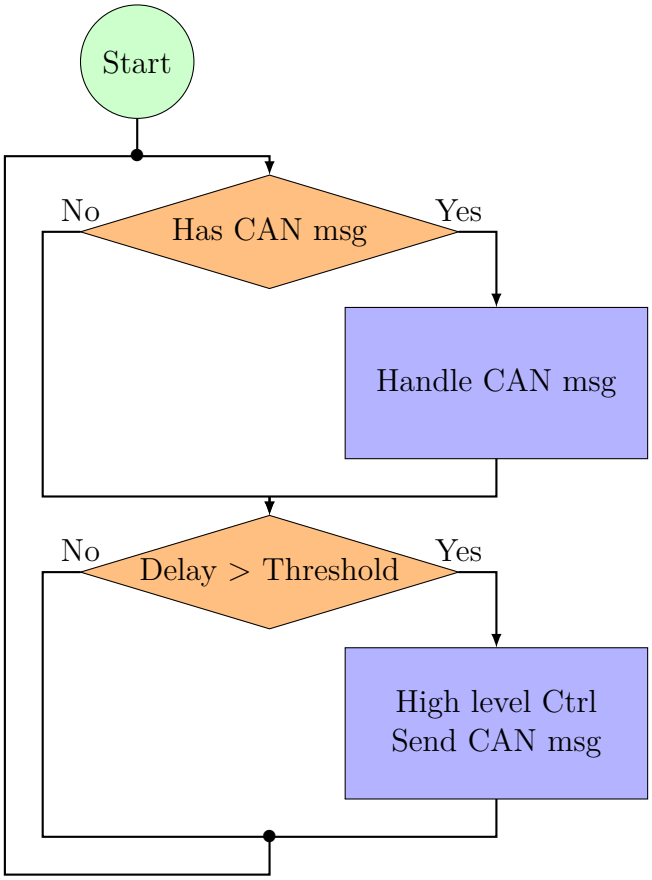


Figure 4.6: Flow chart diagram of the high-level controller on the computer.

4.4.3 Physical layout

The new electrical wiring of the eel-robot is shown on FIGURE 4.7. The Dynamixels were kept daisy-chained (orange) for simplicity. The encoders need 5 V to work and

are also daisy-chained, but their data I/O must be kept separated. The powering of the robot was done with a DC power supply unit, and the communication was realised on a CAN bus to ensure the robustness of communication.

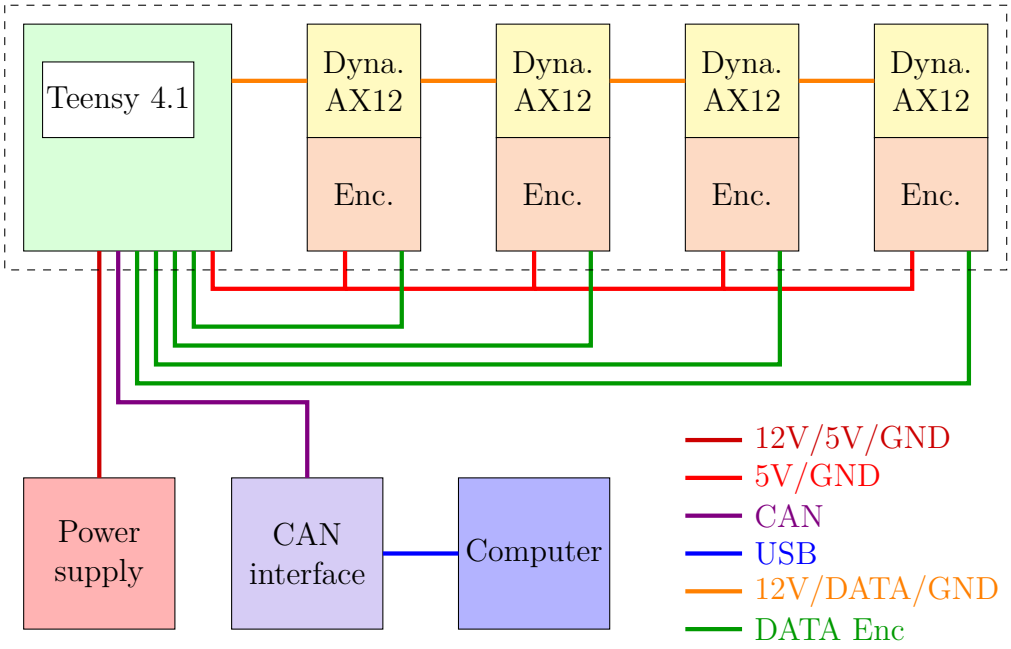


Figure 4.7: Wiring schematic of the eel robot. The onboard components are inside the dashed rectangle.

The PCB (Figure B.1) has 5 main parts:

- The microcontroller
- The level shifter for the encoders
- The TTL communication circuit for the Dynamixels
- The CAN transducer to send message on the CAN bus
- The LEDs for status.

The LEDs were used as a status display for the different voltage inputs as well as various other relevant program states.

Chapter 5

Validation

5.1 SEA

5.1.1 Static validation

This experiment aims to quantify the accuracy and eventual non-linearities of the SEA's torque measurement.

Method To validate the SEA's torque measurement, we compared the estimated torque τ_{SEA} with an independent measure. We used two different measurement tools:

- A dynamometer: the experimental setup is shown on FIGURE 5.1 (left): the dynamometer measures the force applied by the SEA on a lever arm. By knowing its length L_d, we can compute the output torque τ. We used two different values for L_d to make better use of the measurement range of the dynamometer. However, the dynamometer is accurate only up to 0.1 N, and we had to ensure the lever arm was perfectly horizontal, which led us to look for another, more precise way to measure the torque.
- A precision scale: the experimental setup is shown on FIGURES 5.1 (right) and 5.2. The scale is accurate up to 1×10^{-4} N, and the principle is the same as for the dynamometer. However, it is much more precise, and we did not need to ensure the horizontality of the lever arm as we could consider the vertical displacement of the scale to be zero.

Results The results are shown on FIGURE 5.3. Evidently, the springs exhibit clear linear behaviour up to 90°, which is to be expected as the stiffness changes at this point due to the spring disposition in the SEA design. However, we also observe

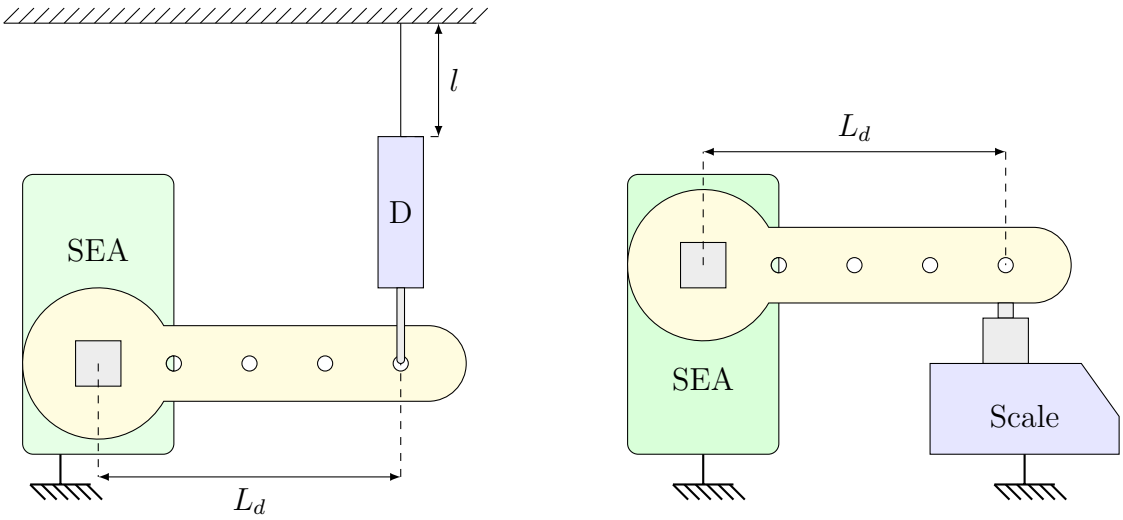


Figure 5.1: Scheme of the experimental static validation of the SEA. Left is the experiment with the dynamometer. Right is the experiment with the scale.

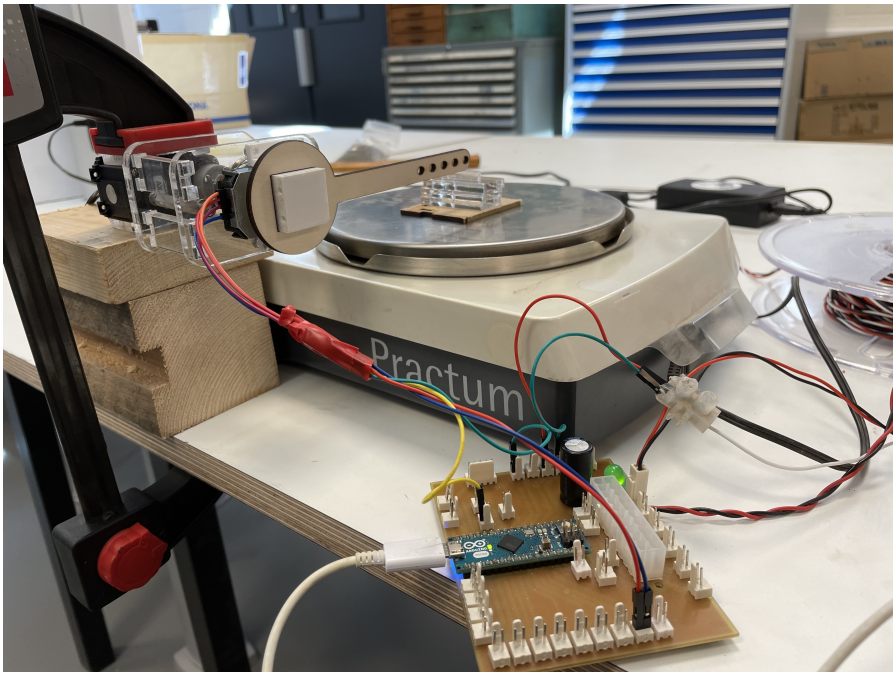


Figure 5.2: Setup for the test on the precision scale for the static validation.

a slight difference (about 10 %) between the measured value and the predicted value. This is most likely due to slight stiffness variations between the spring datasheet and the real spring.

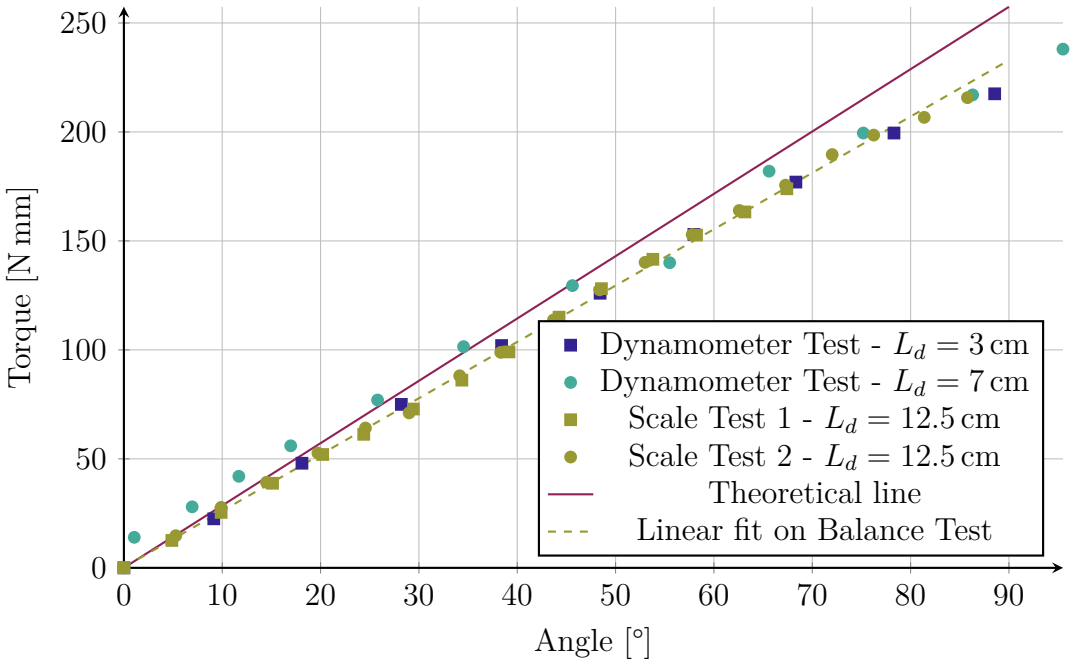


Figure 5.3: Measured torque of the SEA for different angular deflection on the dynamometer test and scale test compared to the theoretical torque.

Discussion Avoiding the 10 % error on the sping stiffness constant is easy enough: each SEA spring set simply needs to be properly characterized by following the same experiment. In practice, we elected not to do so and to consider the theoretical (datasheet) stiffness as accurate due to time constraints.

5.1.2 Dynamic validation

The objective of this experiment is to measure the SEA's operational bandwidth.

Method We imposed a sine reference position of variable frequency at the input of the Dynamixel, thus simulating a reference torque (as the torque is directly proportional to the position):

$$\theta_M(t) = \frac{\pi}{3} \sin(2\pi f t) \tag{5.1}$$

The amplitude choice was made to cover the main part of the work zone. We solidarized the input (Dynamixel) with the output of the SEA so that the only moving parts were the springs and the attached axis, as shown in FIGURE 5.4.

We also performed the same experiment on the Dynamixel without the spring to compare the bandwidth of the SEA with that of the Dynamixel.

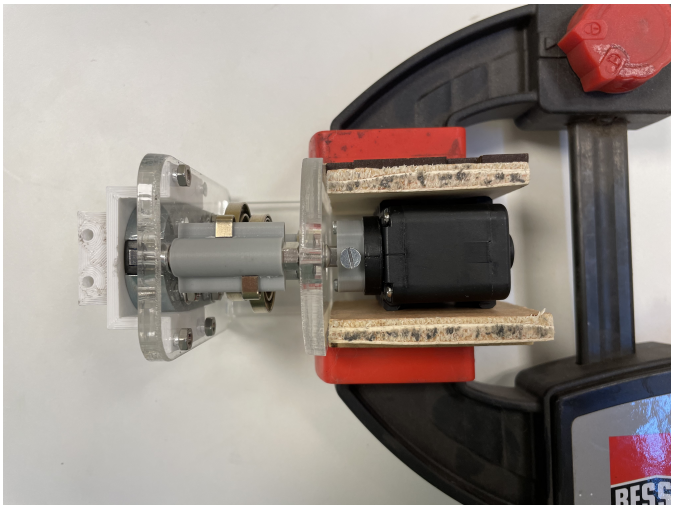


Figure 5.4: Experimental setup for the dynamic SEA validation. The output of the SEA is solidarised with its input, the Dynamixel.

Results The bode plot (amplitude and phase) is shown on FIGURE 5.5. Evidently, the limiting factor is the Dynamixel, as the bandwidth of the SEA is exactly the same as that of the Dynamixel. We find a bandwidth value of 1.35 Hz, which is small but enough for the eel-robot as the frequencies involved are around 0.2 Hz, as defined earlier.

5.2 Middle-level torque controller

Method The middle-level torque controller is implemented as a PID controller:

$$C_{\text{PID}}(s) = K_{\text{P}} + \frac{K_{\text{I}}}{s} + K_{\text{D}}s \tag{5.2}$$

We tuned the gains by the successive application of two methods:

- Ziegler-Nichols' rule: this method consists in finding the critical gain K_{u} of a simple proportional controller. To do so, the gain K_{P} needs to be increased until reaching the stability limit of the system. This stability limits defines K_{u} and T_{u} (where T_{u} is the oscillation period). Knowing those, we compute the PID gains as:

$$\begin{aligned} K_{\text{P}} &= 0.2K_{\text{u}} \\ K_{\text{I}} &= 0.4K_{\text{u}}/T_{\text{u}} \\ K_{\text{D}} &= 0.667K_{\text{u}}T_{\text{u}} \end{aligned}$$

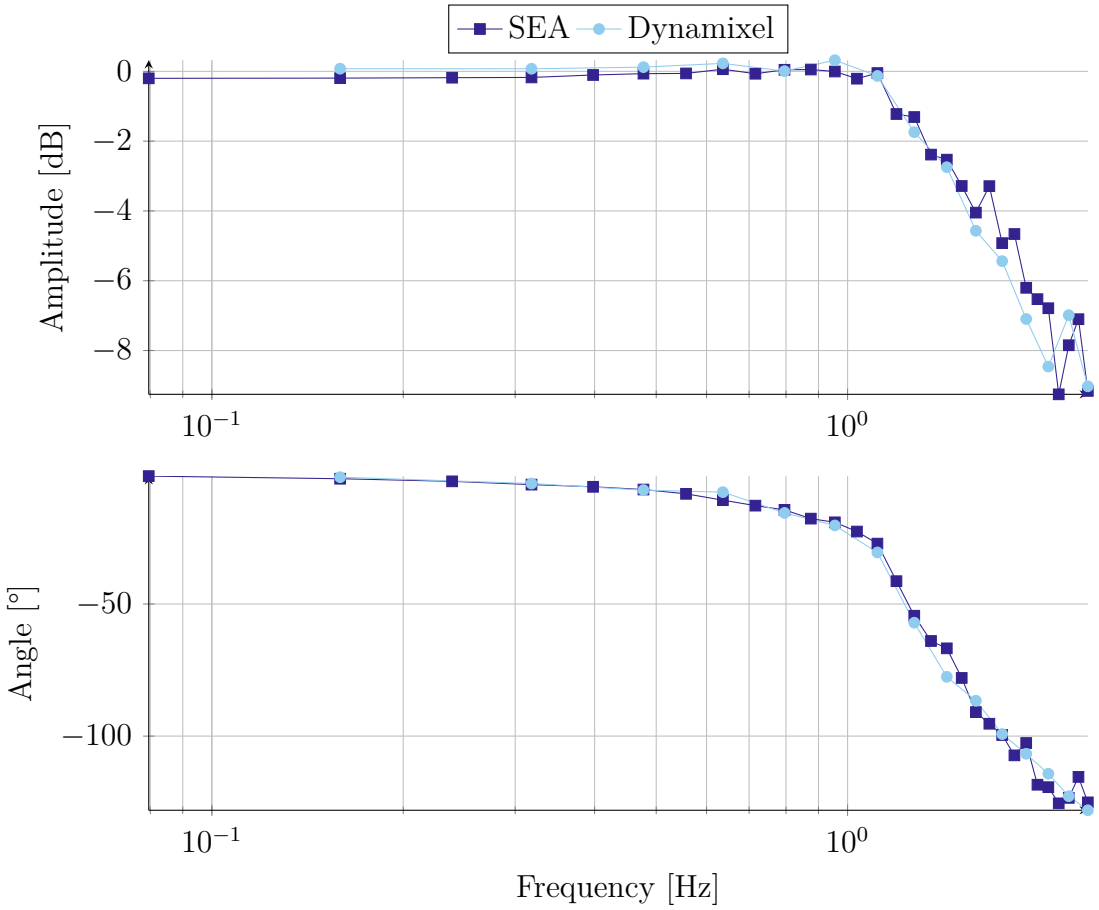


Figure 5.5: Bode diagram for the SEA's frequency response. Above is the amplitude diagram and below is the phase diagram.

which is a slightly modified "no-overshoot" rule, allowing for less aggressive gains that are, supposedly, less prone to overshooting [27].

- Rules of thumb: this is by no means an exhaustive or rigorous mean of tuning a PID controller, but small gains in performance can be obtained by hand-tuning gains while keeping in mind some key points:
  - Increasing K_{P} and K_{D} generally accelerates the system's closed-loop response, though at the cost of overshoot and oscillations if increased too aggressively.
  - The integral gain K_{I} allows to cancel any static error. Higher values generally improve the overall system tracking of the error.

Results The obtained controller step response is shown at FIGURE 5.6. The no-overshoot Ziegler-Nichols rule was a good starting point for further "rules of thumb" tuning, although it exhibited an overshoot contrarily to what its name might suggest. The closed-loop response's settling time of order $\sim 0.25\,\mathrm{s}$ which is good enough with respect to the position control period of $T = 5\,\mathrm{s}$.

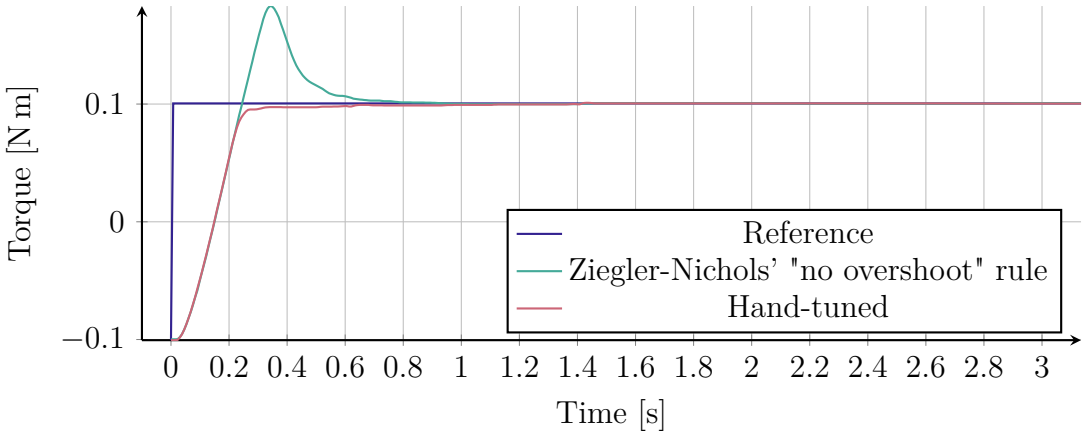


Figure 5.6: Torque controller response to a step.

5.3 High-level position controller

5.3.1 Feedback position controller

Method The feedback position controller is implemented as a PID controller, and the gain tuning procedure was exactly the same as for the middle-level torque controller.

Results The results of the step response is shown at FIGURE 5.7. When trying the obtained controller for a sine reference setpoint, the result thus obtained was really poor. This difference between a step response and a sine reference tracking is likely due to the slowness of the settling time compared to the sine period of $T = 5\,\mathrm{s}$. To try and alleviate this issue, we tried to further hand-tune the gains and obtained the result shown at FIGURE 5.8. While it remains somewhat acceptable in terms of performance, the tracking error is never cancelled.

Discussion The poor performances of the high-level position control in terms of error tracking might simply be due to the intrinsic properties of the two-link

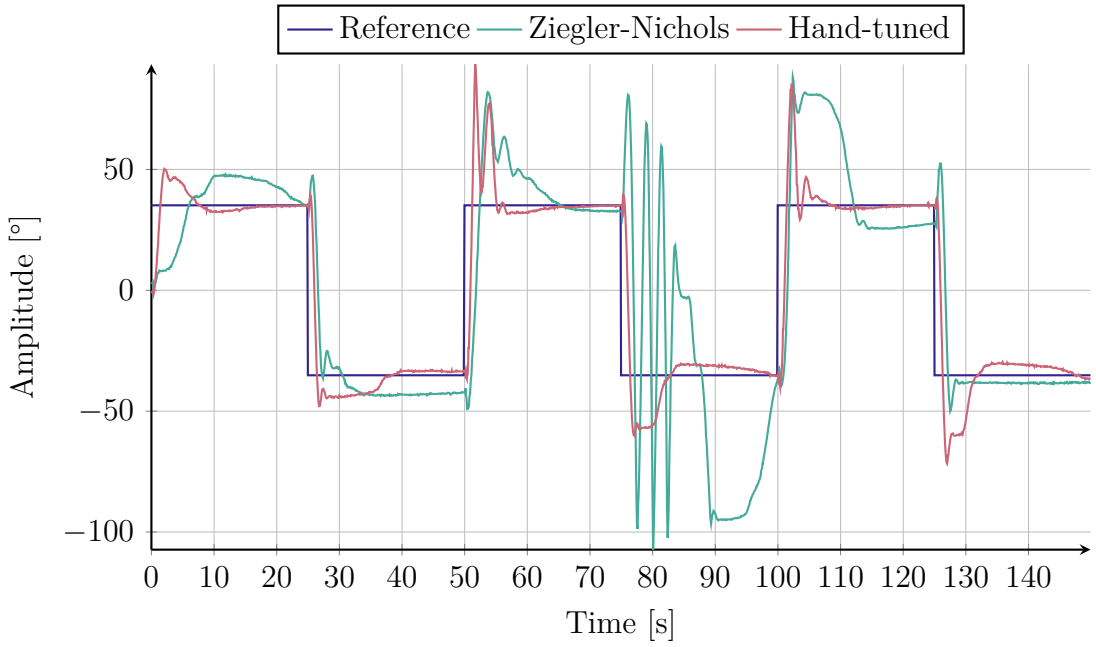


Figure 5.7: Position controller response to a step reference with a frequency on a single section.

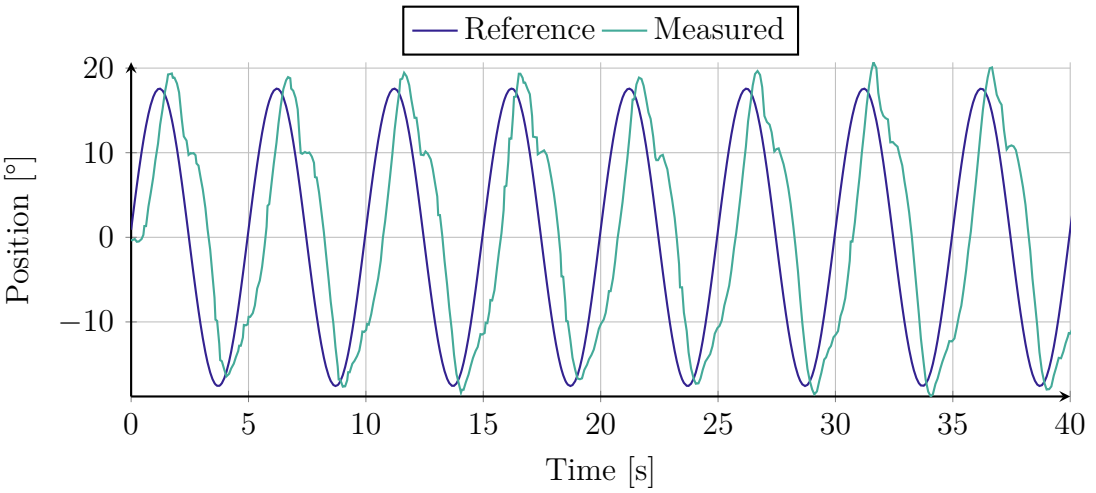


Figure 5.8: Position controller response to a sine reference with frequency $\nu = 0.2\,\text{Hz}$ on a single section.

system. However, we believe better performances might be achieved by using a

proportional-resonant (PR) controller as an alternative to the PID controller:

$$C_{\mathrm{PR}}(s) = K_{\mathrm{P}} + \frac{K_{\mathrm{I}} s}{s^2 + \omega_0^2} \tag{5.3}$$

where $\omega_0 = 2\pi\nu$ is the resonant frequency. Indeed, as the settling time of the PID controller is not "much faster" than the fundamental frequency $\nu = 0.2\,\mathrm{Hz}$ of the system, it is unable to cancel the error due to the lack of infinite gain at this frequency (instead, PID controller have infinite gain at the DC frequency, which is why they can successfully cancel the static DC error).

Historically, the control of AC quantities (such as the PWM signals in power electronics components) is made by using PI controllers in the so-called "synchronous" or "dq" frame with the help of the Park transform, which is essentially equivalent to using a PR controller in the fixed frame. However, for single-phase PI control, this transformation procedure cannot be applied directly. More details about this can be found in [28] and the references therein.

In practice, the digital implementation of such a controller is not as straightforward as that of a PID or PI controller, as detailed in [28, 29] and might require further investigating.

5.4 Two-link system

This section summarises the controller experiments made on a two-link system in the air. For simplicity reasons, we decided to first validate the controller in the air instead of in the water and with less sections than the normal eel-robot (5 sections and 4 joints). The presented experiments and results, while not entirely representative of the robot's behaviour when it is under-water, should still serve as a good validation of our work.

The experimental setup is shown at FIGURE 5.9. We will refer to the articulation closest to the table as the "proximal joint" and the furthest as the "distal joint".

5.4.1 Feedback only

Method For this experiment, the feedforward contribution of the high-level position controller was set to zero. The reference position was chosen as the CPG control law (2.2) with a slightly increased amplitude to further test the system's limits.

Results When using a frequency of $\nu = 0.2\,\mathrm{Hz}$, we observed the system to be unstable and very hard (or even impossible) to control. Subsequently, we decreased the frequency to $\nu = 0.1\,\mathrm{Hz}$ and the results are shown on FIGURES 5.10 and 5.11.

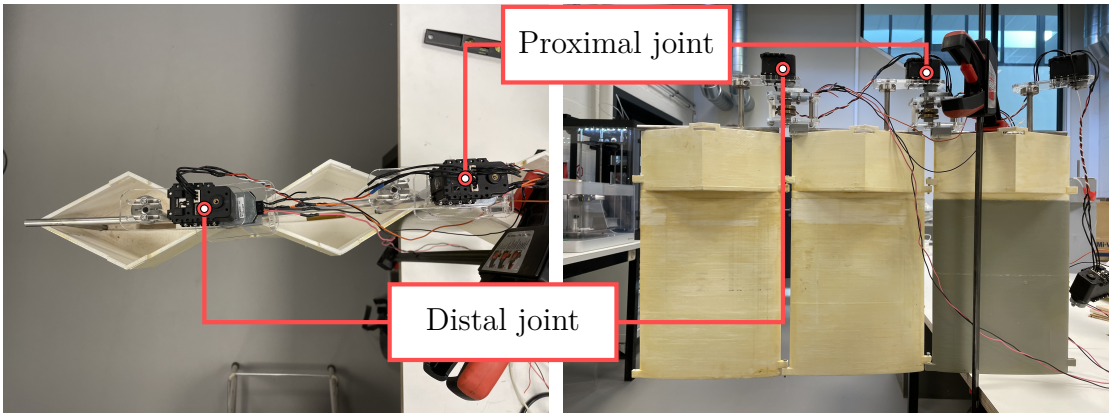


Figure 5.9: Experimental setup for the two-link system with the side view (left) and top view (right).

While it exhibits acceptable position tracking, the tracking error is non-zero both for position and torque, and the overall controlled system is very sensitive to outside perturbations, exhibiting unstable behaviour whenever it is perturbated.

Discussion Overall, the pure-feedback controller has very poor performances and stability properties. The remaining question is: can it be improved to be able to reach dynamics around $\nu = 0.2\,\text{Hz}$, which is that of the eel-robot? We believe performances might be improved by the use of a PR controller instead of a PID for the high-level controller, but it remains to be demonstrated.

5.4.2 Feedforward and feedback

Method The methodology followed for this experiment is the same as for the feedback-only experiment, but one detail: the feedforward torque was non-zero. However, finding the right phase and amplitude is a non-trivial matter. Due to the lack of exploitable data, we elected to follow a heuristic approach; a potentially more rigorous mean of extracting that information will be discussed later.

The following recipe was applied to both the distal and proximal articulations successively until suitable phase, and amplitude parameters were found:

- Focus on one articulation and maintain the other fixed;
- Start with ϕ^0 and A^0 (where an initial amplitude guess can be suitably determined based on experimental observations of pure feedback control);
- Adapt ϕ until the feedback contribution becomes minimal;

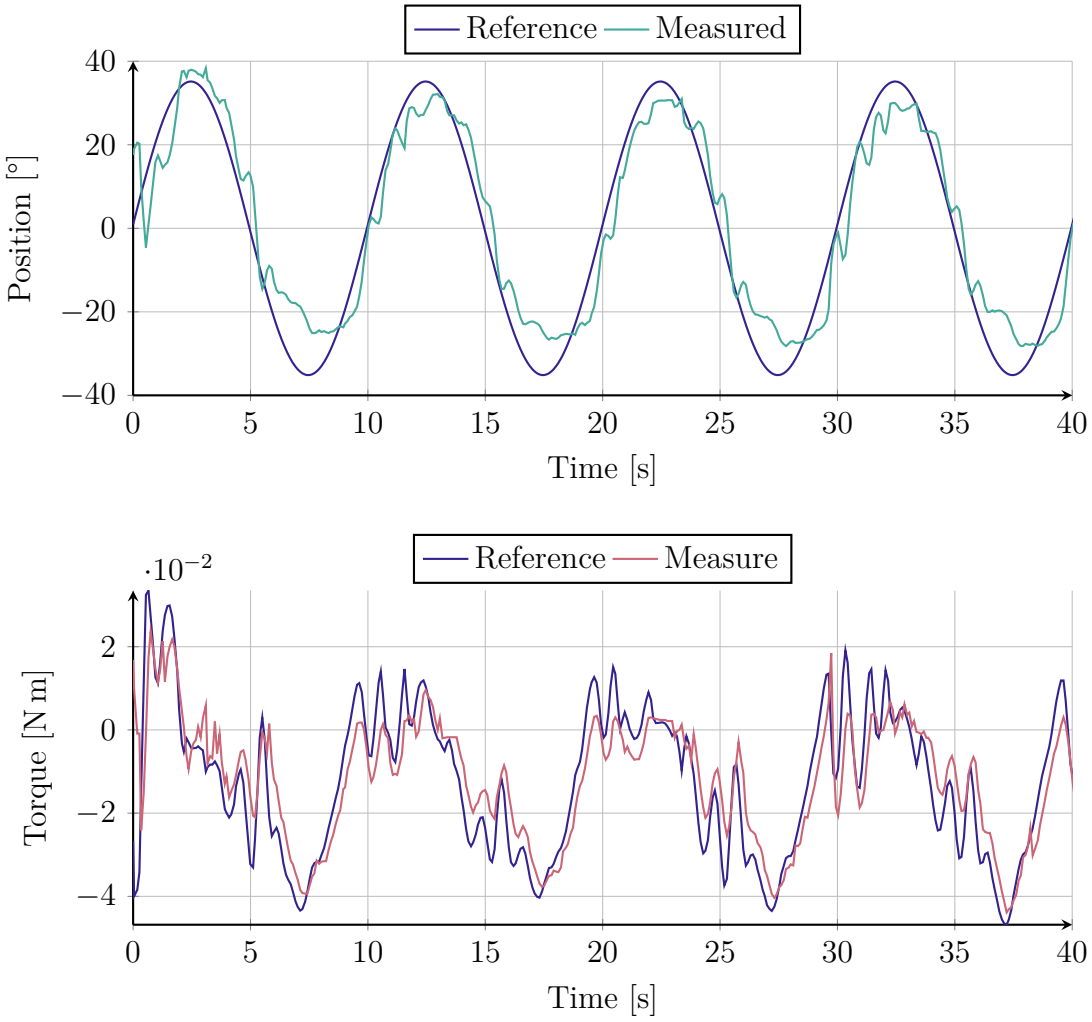


Figure 5.10: Position reference and measure of the distal articulation in a two-link pure-feedback experiment setup. Also shown are the reference and measured torque.

- Once a good phase is found, adapt the amplitude until the feedback contributions become minimal;
- Repeat the two previous step until satisfied with the result.

Once both feedforward torque is tuned for each section individually, further minor changes can be applied to the phase and amplitude. Again, however, those should be minimal. In practice, we had no difficulty obtaining good results by following this procedure and had too few modifications once each section was tuned individually.

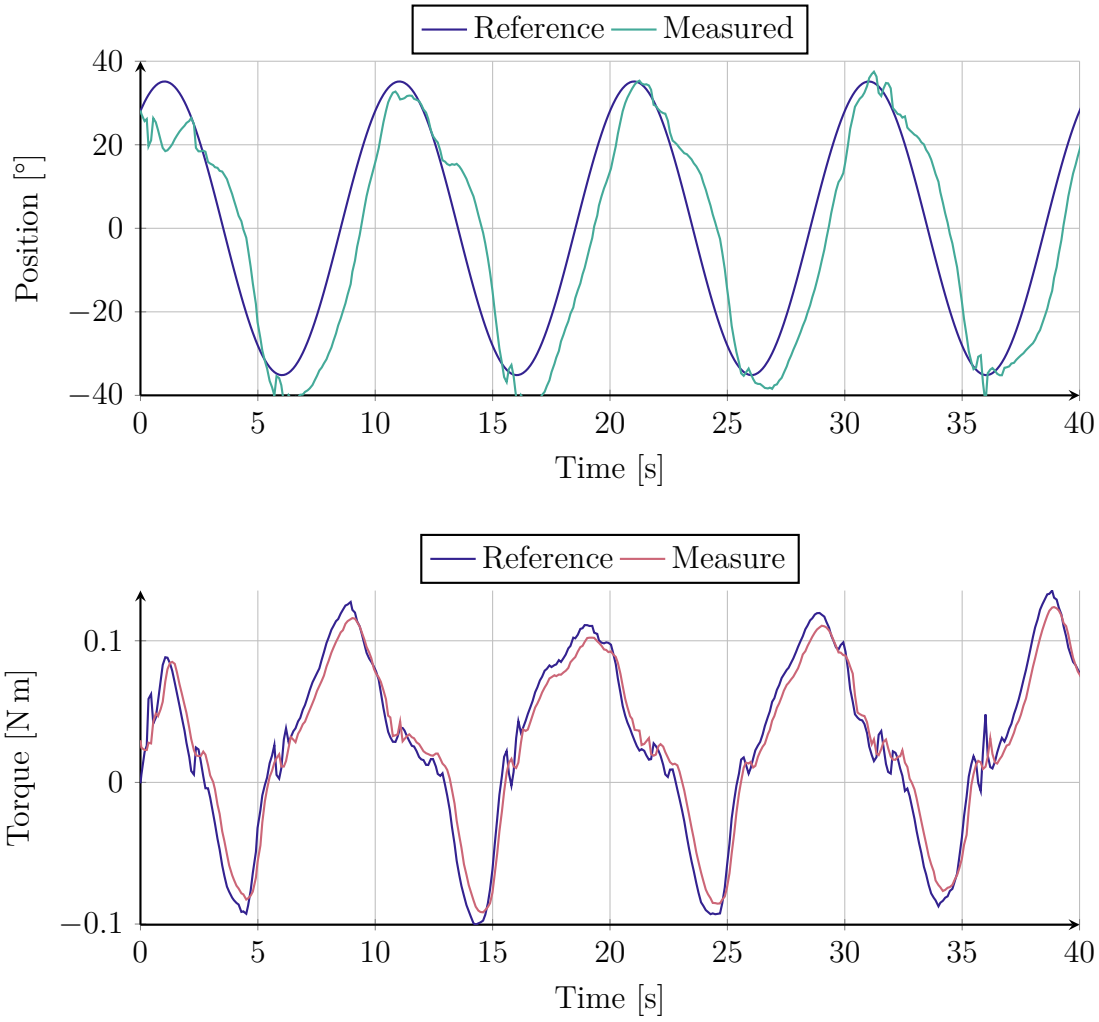


Figure 5.11: Position reference and measure of the proximal articulation in a two-link pure-feedback experiment setup. Also shown are the reference and measured torque.

Results The results are shown on FIGURES 5.12 and 5.13. As expected, we observe that the feedback contribution becomes smaller with respect to the feedforward contribution as it only needs to stabilize the slight deviation inherent to a pure feedforward controller. This is especially true for the proximal articulation, where the feedback contribution is orders of magnitude smaller than the feedforward contribution.

The stability of the controller is also greatly improved, as it is much more robust to a perturbation than the pure feedback controller. Indeed, whenever a perturbation is applied, the feedback contribution rises in magnitude and corrects

the trajectory until brought back to a stable regime.

The overall controller bandwidth is also improved, as we can easily reach $\nu = 0.2\,\mathrm{Hz}$, whereas we were limited to at best $0.1\,\mathrm{Hz}$ for pure feedback control, with much poorer tracking performance.

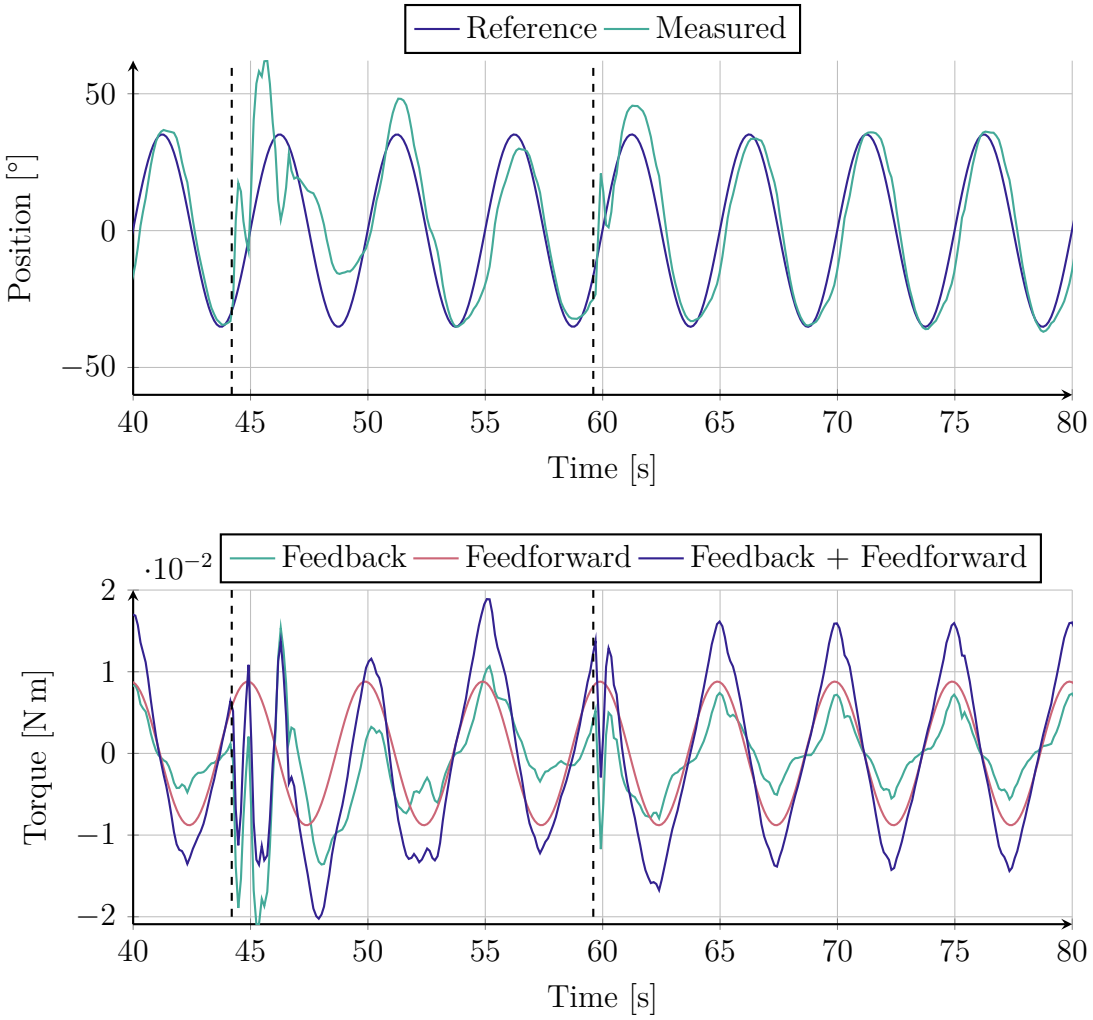


Figure 5.12: Position reference and measure of the distal articulation in a two-link experiment setup. Also shown are the two contributions of the high-level position controller (feedback and feedforward) and their sum. Perturbations are denoted by a dashed line.

Discussion While the obtained results are much better than for pure feedback control; its quality heavily relies on finding a good approximation of the feedforward torque. The methodology we presented works fairly well for simple two-section

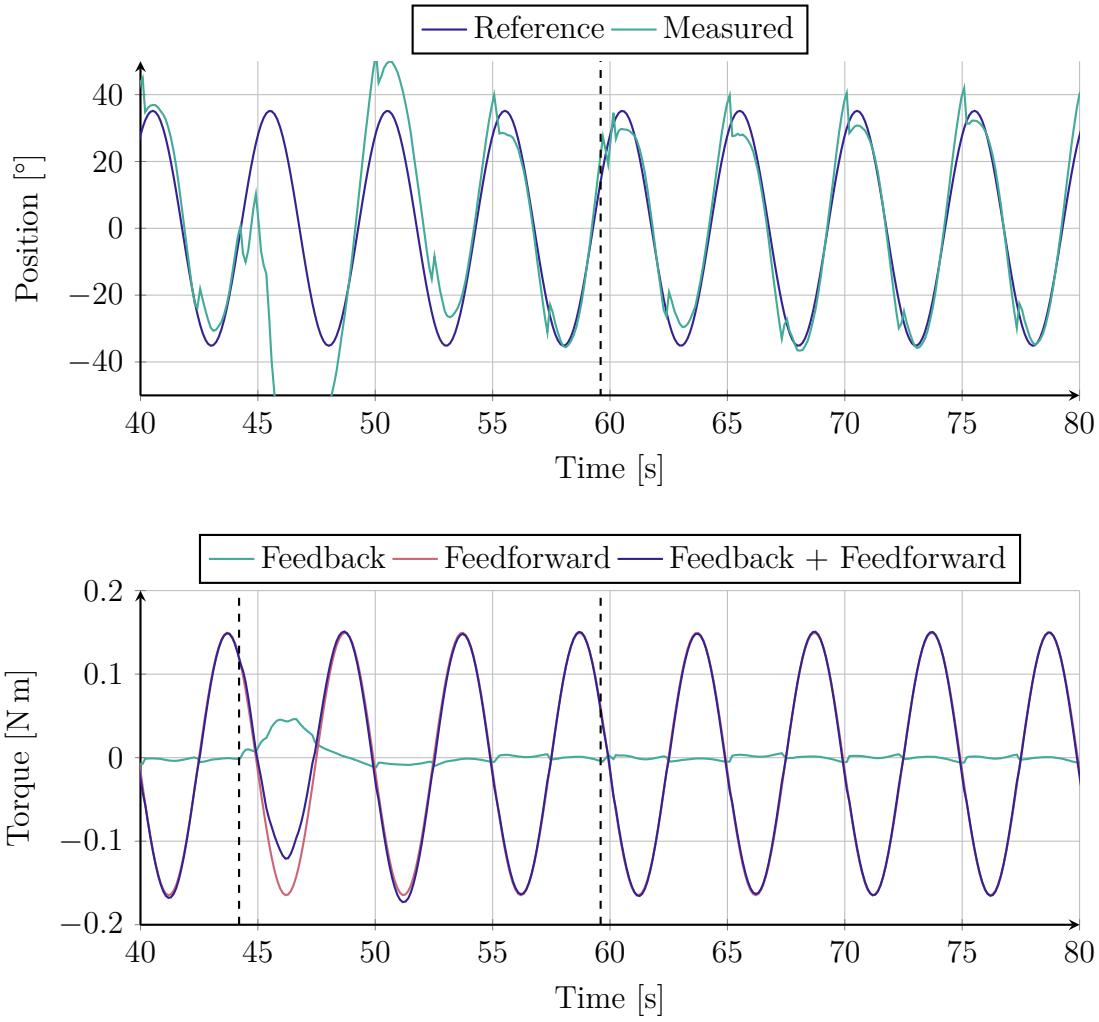


Figure 5.13: Position reference and measure of the proximal articulation in a two-link experiment setup. Also shown are the two contributions of the high-level position controller (feedback and feedforward) and their sum. Perturbations are denoted by a dashed line.

cases but is likely to be more complicated to apply to a full eel-robot with four sections in the water.

However, there is another approach to compute a good approximation of the feedforward torque, using spectral analysis:

- Obtain good measurements of the torque generated by each joint (either by using the pure-feedback controller, a CFD simulation or else);
- Compute the discrete Fourier transform (DFT) of the obtained torque and

look for the amplitude A_i and phase ϕ_i of the first harmonic $\nu_1 = \nu$ for the i-th joint;

- Compute the approximated torque using the following formula:

$$\tau_{\text{FF},i} \approx 2A_i \cos\left(2\pi\nu + \phi_i\right) \tag{5.4}$$

- Should it prove necessary, subsequent harmonics can also be included to obtain a better approximation of the torque. However, in practice, a simple first harmonic approximation of the torque in a two-link system proved good enough, as seen on FIGURE 5.14.

We applied this procedure to the data obtained during the feedforward two-link system experiment to test our procedure, and the results are shown at FIGURE 5.15.

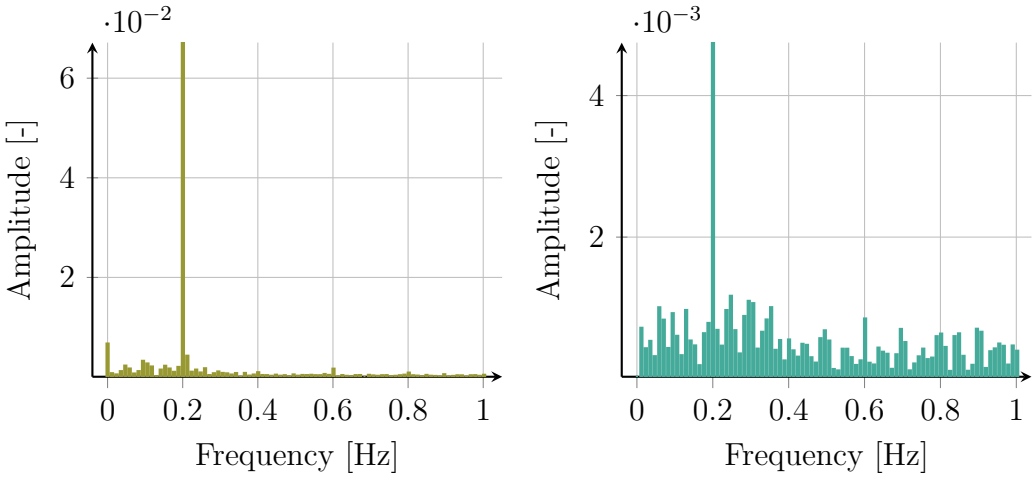


Figure 5.14: Magnitude of the frequency spectrum of the measured torque for both joints of a two-link system in the air. On the left, the proximal joint and on the right the distal one.

We can conclude two things from this:

- The described spectral approximation procedure works very well, as shown for the proximal articulation. The spectrally approximated feedforward torque is very close to the heuristic approximation and even closer to the measured torque.

- The heuristic approach actually yielded poor results for the distal articulation. Indeed, the phase shift of the spectral approximation is different (and better

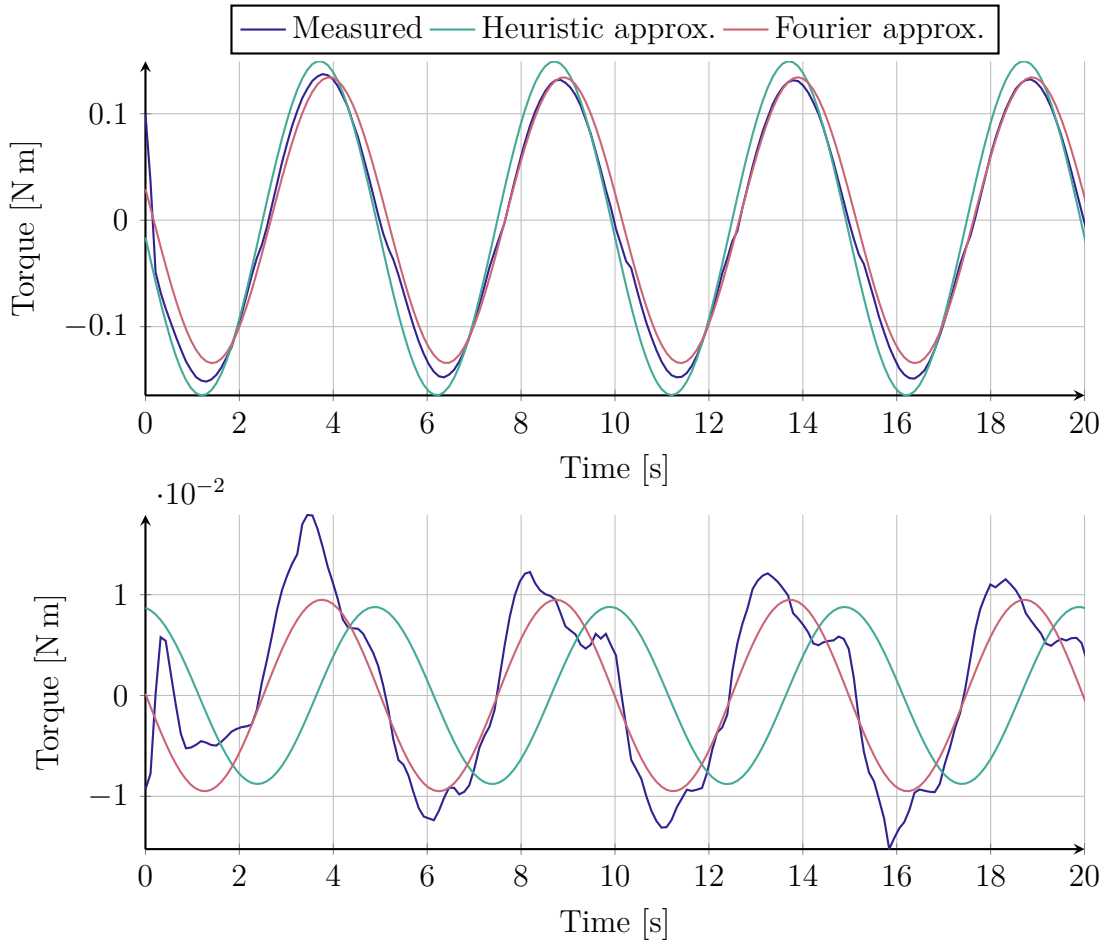


Figure 5.15: Torque approximation methods for a two-link system in the air with $\nu = 0.2\,\mathrm{Hz}$. Above, the proximal joint and below the distal one.

fits the measured torque) than that of the heuristic approximation. It shows that considering each joint separately does not allow to account for any coupling effect that may arise, thus modifying the required phase shift.

However, the second and more rigorous approach does not work well when the torque data is not known a priori or of poor quality. In our case, we could not apply this procedure since the pure feedback controller does not work well at al at $\nu = 0.2\,\mathrm{Hz}$.

Chapter 6

Conclusion

In this work, we presented a new compact and easily adjustable design for a Series Elastic Actuator. Its spring stiffness can easily be adapted (given the catalogue availability) to fit a given situation, as only minor modifications are required to adjust to a new spring. The current design can work in ranges of $\tau = R \times 80°$ and its accuracy can be adapted to the need of any application. Its dynamic capabilities, however, are currently limited by the bandwidth of the Dynamixel to about 1 Hz but could be extended further by using another actuator. The actual cost of one SEA is about 100€.

We also replaced the old joints in the eel-robot with the new SEA design and designed a controller to handle torque control. Currently, we are still working with a position-based control law, but the joint is torque-controlled. We successfully applied our controller to a two-link testbench.

We obtained poor stability results in the case of pure-feedback stabilising position control. We think this part of the controller could be improved using a Proportional-Resonant controller, but this has yet to be further investigated. However, by adding a feedforward action, we obtained much better results both in terms of stability, tracking capabilities, and overall attainable control frequencies.

This control has not yet been tested in the water, and some challenges remain to be tackled, but the current results are encouraging. In our opinion, several issues need to be addressed moving forward:

- Investigate a proper method to estimated the joint torque of the eel-robot in the water: we proposed a method based on frequency analysis that looks promising but has yet to be proven. The biggest challenge is obtaining usable data for this analysis. Fortunately, the CFD simulator should prove to be a good start.

- Investigate the limitations of the Dynamixel AX-12 for this kind of torque control. Indeed, we highlighted some delay issues that arose during our work.

These were not too much of a problem in a two-link system but might become one when used on the entire eel-robot, which has at least twice as many articulations.

Lastly, we designed new sections to accommodate colouring agent injection. Unfortunately, we did not have the time to test them in the pool, but two of them are ready to be tested.

Appendix A

Colouring agent

As stated in the Chapter 1.2, one objective of the project is to compare the experimental result to the CFD's simulator. The measurement of the robot position was already realised in the second iteration, but we still lack measurement of the flow. For that purpose, we want to use Particle image velocimetry. So we need to inject a colouring agent (tracing particle) near the middle height of a section (to avoid edge effects). We could do it by hand, but it will also add perturbation, so we would prefer to do it remotely from the robot.

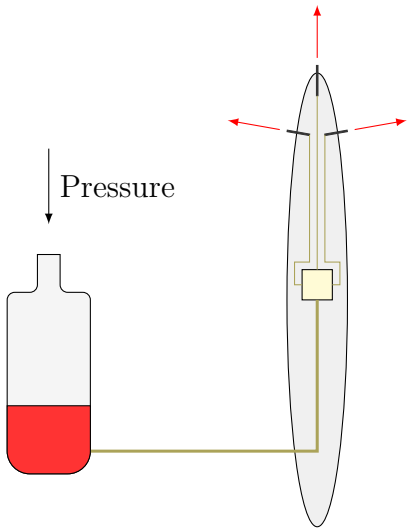
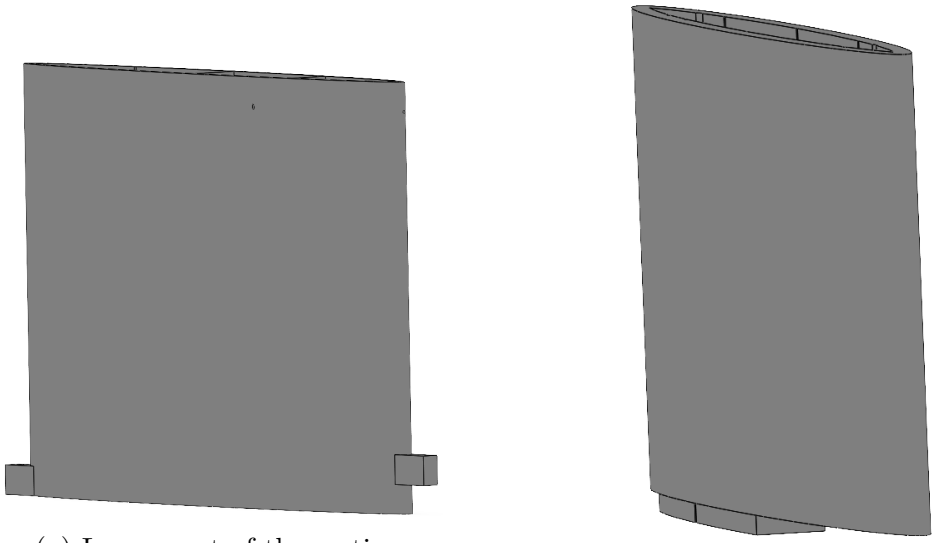


Figure A.1: Schematic principle of the colouring agent injection in a section of the robot.

The hall LEFT already experimented with colouring agent injection, so we simply implemented their solution for the robot (Figure A.1). We have a container with the colouring agent (red) with input for pressured air and an output. Pressure

can be injected into the container from the pool control board. It will push the colouring agent through small tubing into an X fitting. The output of this fitting is connected to a small needle inserted into the section.

The sections needed modification to have the needle inserted. The opening is too narrow to work at the middle height of the section. So it was redesigned in two parts (FIGURE A.2): the bottom one with small holes for the needles and the upper one with a matching connector for the assembly of the two parts. The assembly will be done with a PLA solvent glue to ensure water tightness.



(a) Lower part of the section

(b) Upper part of the section

Figure A.2: New CAD model of the section with the holes for the needles and the matching connector.

As the sections needed to be reprinted, we also made other improvements. The thickness of the wall was reduced, but some cross-sections were needed to prevent deformation. This modification should help the waterproofing of the section and help lower the centre of mass with the ballast. The sections are 3D printed, and the waterproofing is defined by the number of walls. We could not have more than three walls on the inside and outside in the previous design. Otherwise, the weight would increase too much. By reducing the width, we can use the three walls of the inside and outside to have six walls. The mains components (FIGURE A.3) of those sections are:

1. Pin hole for the assembly of two sections
2. Hole to maintain the tube from the transmission

3. Holes for the needle insertion
4. Connector for an easier assembly
5. Cross sections for the rigidity of the structure
6. Conduct to allow the tube from the transmission

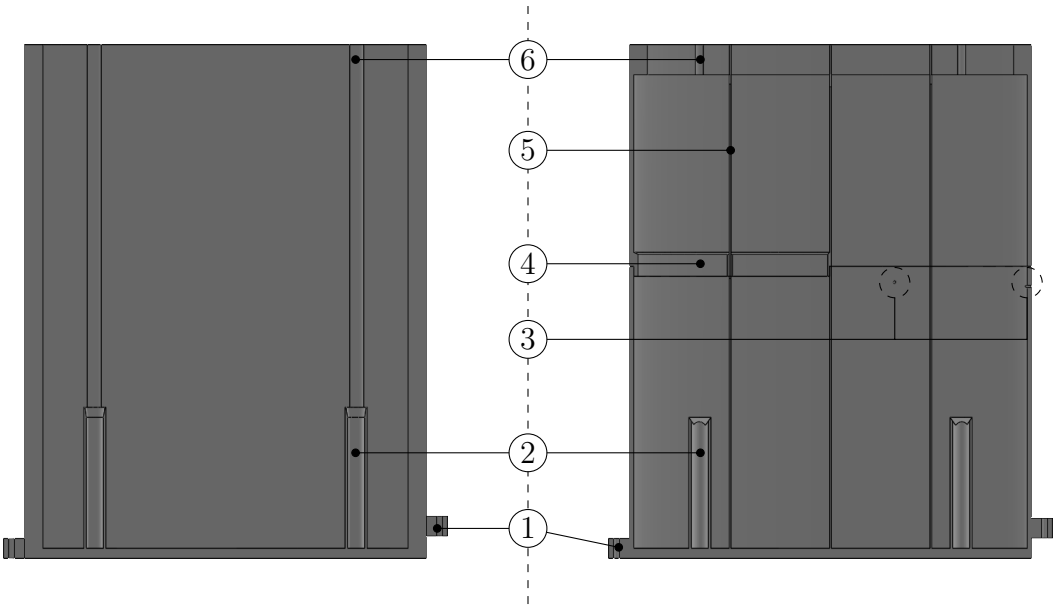


Figure A.3: Sectionnal view of the old section (left) and the new section (right) for the colouring agent injection.

The test of the system with the robot was ultimately not realised due to time constraints.

Appendix B

Hardware

B.1 Cost of the SEA

Name	Price [€]
Encoder	19,47
Spring	28,60
D-cut shaft	11,49
Ball bearings	4,46
Crosspiece	6,48
M3 nut	5.22
Socket screws	2,83
M3 washers	3,3
M3 bolt	5,58
M2 bolt	3,04
Shaft Collars	7,81
Total:	98.66

Table B.1: Price list of the SEA for the off-the-shelf components.

B.2 Electronics

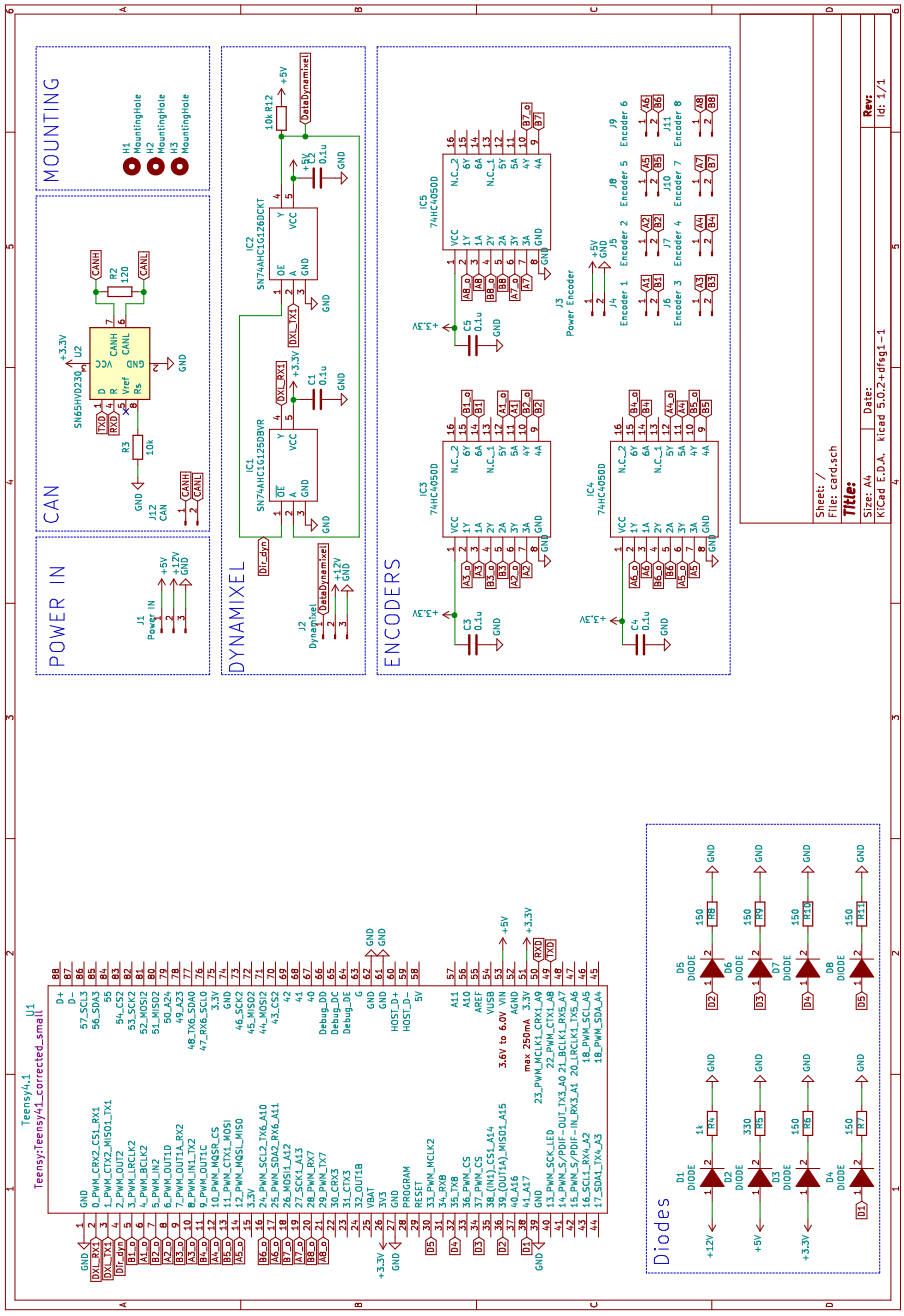


Figure B.1: Schematic of the pcb for the Teensy inside the robot.

List of Figures

1.1 Swimming mode associated with a Body and/or Caudal Fin (BCF) propulsion. Adapted from [1]. 7
1.2 Ostraciidae fish (left), bio-mimetic ostraciiform underwater robot (right) [2]. 8
1.3 Robotuna on display at the MIT Museum [3]. 8
1.4 Assembly of the transmission system (tail and fin) and the thunniform robot fore-body [4]. 9
1.5 G6 Carangiform robot from Essex Robotics Research [5]. 9
1.6 Lamprey robot developed by the the Northeastren University [6]. . 10
1.7 REEL II by Kenneth A. McIsaac and James P. Ostrowski [6]. . . . 11
1.8 Eel robot from the ROBEA project [8]. 11
1.9 Snake-like robot ACM-R5 from Hirose-Fukushima Robotics Lab [9]. 12
1.10 ANGELS robot with nine module [10]. 12
1.11 Robot made during the Lampetra project [12]. 12
1.12 Amphibot III from the EPFL [13]. 13
1.13 Pleurobot robot from the EPFL [15]. 14
1.14 Representation of the eel robot (in red) in the CFD simulator. . . . 14
1.15 CAD representation of the eel-like robot at the end of the first iteration. 15
1.16 CAD representation of the eel-like robot at the end of the second iteration. 15

2.1 CFD simulation of the sine control law (2.1). Joint positions and torque are shown for five sections and four articulations. 18
2.2 Schematic representation of the two chains of oscillators of a CPG. 18
2.3 CFD simulation of the CPG control law. Joint positions and torque are shown for five sections and four articulations. 19
2.4 CFD simulation of a pure feedforward torque control law, following the torque generated by the CPG position control law. Joint positions and torque are shown for five sections and four articulations. 20

3.1 Scheme of current measurement to evaluate the torque. 23
3.2 Scheme of the electrical power method to evaluate the torque. . . . 24

3.3 Scheme of reaction torque measurement. 25
3.4 Scheme of direct torque measurement. 26
3.5 Scheme of a series elastic actuator to evaluate the torque. 26
3.6 Max (plain line) and mean (dashed line) power computed with the data of the simulation with the CPG law of control for different stiffness of spring. 29
3.7 Power ratio of the SEA for different resolution for the torque measurement. 30
3.8 SEA design based on compression springs and bowden cable from [23]. 31
3.9 SEA design based on compression spring in a circular housing with a deflection of 5° from [24]. 32
3.10 Monolithic SEA design based on FEM optimisation from [25]. . . . 32
3.11 View of the CAD assembly of the SEA. 33
3.12 Picture of the final SEA with a ruler for a length comparison. . . . 34
3.13 Sectional view of the CAD assembly of the SEA. 35
3.14 Sectional view of the CAD model of the old transmission (left) and the new one (right) with the list of main components. 37

4.1 General block diagram of the SEA controller. 38
4.2 Schematic of the low-level controller implemented on the Dynamixel. 39
4.3 Schematic of the middle-level torque controller implemented on the Teensy. 40
4.4 Schematic of the high-level position controller implemented on the computer. The feedback part is shown in blue and the feedforward is shown in red. 41
4.5 Flowchart of the middle-level controller implemented the Teensy. . . 42
4.6 Flow chart diagram of the high-level controller on the computer. . . 43
4.7 Wiring schematic of the eel robot. The onboard components are inside the dashed rectangle. 44

5.1 Scheme of the experimental static validation of the SEA. Left is the experiment with the dynamometer. Right is the experiment with the scale. 46
5.2 Setup for the test on the precision scale for the static validation. . . 46
5.3 Measured torque of the SEA for different angular deflection on the dynamometer test and scale test compared to the theoretical torque. 47
5.4 Experimental setup for the dynamic SEA validation. The output of the SEA is solidarised with its input, the Dynamixel. 48
5.5 Bode diagram for the SEA's frequency response. Above is the amplitude diagram and below is the phase diagram. 49
5.6 Torque controller response to a step. 50

5.7 Position controller response to a step reference with a frequency on a single section. 51
5.8 Position controller response to a sine reference with frequency $\nu = 0.2\,\text{Hz}$ on a single section. 51
5.9 Experimental setup for the two-link system with the side view (left) and top view (right). 53
5.10 Position reference and measure of the distal articulation in a two-link pure-feedback experiment setup. Also shown are the reference and measured torque. 54
5.11 Position reference and measure of the proximal articulation in a two-link pure-feedback experiment setup. Also shown are the reference and measured torque. 55
5.12 Position reference and measure of the distal articulation in a two-link experiment setup. Also shown are the two contributions of the high-level position controller (feedback and feedforward) and their sum. Perturbations are denoted by a dashed line. 56
5.13 Position reference and measure of the proximal articulation in a two-link experiment setup. Also shown are the two contributions of the high-level position controller (feedback and feedforward) and their sum. Perturbations are denoted by a dashed line. 57
5.14 Magnitude of the frequency spectrum of the measured torque for both joints of a two-link system in the air. On the left, the proximal joint and on the right the distal one. 58
5.15 Torque approximation methods for a two-link system in the air with $\nu = 0.2\,\text{Hz}$. Above, the proximal joint and below the distal one. . . 59

A.1 Schematic principle of the colouring agent injection in a section of the robot. 62
A.2 New CAD model of the section with the holes for the needles and the matching connector. 63
A.3 Sectionnal view of the old section (left) and the new section (right) for the colouring agent injection. 64

B.1 Schematic of the pcb for the Teensy inside the robot. 66

List of Tables

3.1 Link between the quantitative criterion and a qualitative scale. . . . 27
3.2 Comparison of solution to measure torque in our robot. 28
3.3 Optimal stiffness for the spring material of the SEA to reach a resolution of 8 bits. 31
3.4 Spring stiffness in the SEA for each articulation. 36
3.5 Comparision of the weight and dimensions between the old and new transmission. 37

B.1 Price list of the SEA for the off-the-shelf components. 65

Bibliography

[1] M. Sfakiotakis, D. M. Lane, and J. Davies, "Review of fish swimming modes for aquatic locomotion," *IEEE Journal of Oceanic Engineering*, vol. 24, pp. 237–252, 1999.

[2] R. Zhang, Z. Shen, and Z. Wang, "Ostraciiform underwater robot with segmented caudal fin," *IEEE Robotics and Automation Letters*, vol. 3, no. 4, pp. 2902–2909, 2018.

[3] (2021) Robotuna - wikipedia. [Online]. Available: https://en.wikipedia.org/wiki/RoboTuna

[4] D. Costa, G. Palmieri, M. Palpacelli, and D. Scaradozzi, "Design of a thunniform swimming robot in a multiphysics environment," in *Advances in Service and Industrial Robotics*, S. Zeghloul, M. A. Laribi, and J. S. Sandoval Arevalo, Eds. Cham: Springer International Publishing, 2020, pp. 257–265.

[5] Z. Zhu, "Essex robotics." [Online]. Available: https://essexrobotics.essex.ac.uk/photos.html

[6] T. Knutsen, J. Ostrowski, and K. McIsaac, "Designing an underwater eel-like robot and developing anguilliform locomotion control," *Harvard University*, 2004.

[7] K. McIsaac and J. Ostrowski, "A geometric approach to anguilliform locomotion: modelling of an underwater eel robot," *Proceedings 1999 IEEE International Conference on Robotics and Automation (Cat. No.99CH36288C)*, vol. 4, pp. 2843–2848 vol.4, 1999.

[8] M. El Rafei, "Commande d'un robot Anguille," Theses, Institut National Polytechnique de Grenoble - INPG, Dec. 2008. [Online]. Available: https://tel.archives-ouvertes.fr/tel-00351003

[9] Futura. (2011) Toutes les photos. [Online]. Available: https://www.futura-sciences.com/tech/photos/robotique-robots-animaux-672/robotique-acm-r5-robot-serpent-4343/

[10] Y. Matar, "Etude expérimentale de la nage anguilliforme : application à un robot biomimétique," Theses, Ecole des Mines de Nantes, Mar. 2013. [Online]. Available: https://tel.archives-ouvertes.fr/tel-00821185

[11] (2021) Project - lampetra project. [Online]. Available: http://www.lampetra.eu/Project.html

[12] (2021) Robots. [Online]. Available: https://www.pinterest.es/pin/167970261076282267/

[13] Amphibot: an amphibious snake robot. [Online]. Available: https://www.epfl.ch/labs/biorob/research/amphibious/amphibot/

[14] A. Crespi and A. J. Ijspeert, "Amphibot II: An amphibious snake robot that crawls and swims using a central pattern generator," *Proceedings of the 9th International Conference on Climbing and Walking Robots (CLAWAR 2006)*, pp. 19–27, 2006. [Online]. Available: http://infoscience.epfl.ch/record/142759

[15] Pleurobot. [Online]. Available: https://www.epfl.ch/labs/biorob/research/amphibious/pleurobot/

[16] "Swimming eel-like robot," https://dial.uclouvain.be/memoire/ucl/object/thesis:10720, accessed: May 2021.

[17] "Swimming eel-like robot : design improvement and control," https://dial.uclouvain.be/memoire/ucl/object/thesis:14899, accessed: May 2021.

[18] A. J. Ijspeert and J. Kodjabachian, "Evolution and development of a central pattern generator for the swimming of a lamprey," *Artificial life*, vol. 5, no. 3, pp. 247–269, 1999.

[19] A. Crespi and A. J. Ijspeert, "Amphibot II: An amphibious snake robot that crawls and swims using a central pattern generator," in *Proceedings of the 9th international conference on climbing and walking robots (CLAWAR 2006)*, no. CONF, 2006, pp. 19–27.

[20] "Dynamixel AX-12A datasheet," https://emanual.robotis.com/docs/en/dxl/ax/ax-12a/, accessed: May 2021.

[21] M. C. Bastos, "High precision current measurement for power converters," *arXiv preprint arXiv:1607.01584*, 2016.

[22] "Ulc ultra low capacity load cell," https://www.interfaceforce.com/products/interface-mini/overload-protected/ulc-ultra-low-capacity-load-cell, accessed: May 2021.

[23] J. F. Veneman, R. Ekkelenkamp, R. Kruidhof, F. Van Der Helm, and H. van der Kooij, "Design of a series elastic-and bowden cable-based actuation system for use as torque-actuator in exoskeleton-type training," in *9th International Conference on Rehabilitation Robotics, 2005. ICORR 2005.* IEEE, 2005, pp. 496–499.

[24] B. Yu, J. de Gea Fernández, Y. Kassahun, and V. Bargsten, "Learning the elasticity of a series-elastic actuator for accurate torque control," in *International Conference on Industrial, Engineering and Other Applications of Applied Intelligent Systems.* Springer, 2017, pp. 543–552.

[25] G. Carpino, D. Accoto, F. Sergi, N. Luigi Tagliamonte, and E. Guglielmelli, "A novel compact torsional spring for series elastic actuators for assistive wearable robots," *Journal of Mechanical Design*, vol. 134, no. 12, 2012.

[26] "Teensy 4.1 development board," https://www.pjrc.com/store/teensy41.html, accessed: May 2021.

[27] "Ziegler-Nichols tuning rule," http://www.mstarlabs.com/control/znrule.html, accessed: May 2021.

[28] R. Teodorescu, F. Blaabjerg, M. Liserre, and P. C. Loh, "Proportional-resonant controllers and filters for grid-connected voltage-source converters," *IEE Proceedings-Electric Power Applications*, vol. 153, no. 5, pp. 750–762, 2006.

[29] A. G. Yepes, F. D. Freijedo, O. López, and J. Doval-Gandoy, "High-performance digital resonant controllers implemented with two integrators," *IEEE Transactions on Power Electronics*, vol. 26, no. 2, pp. 563–576, 2010.

UNIVERSITÉ CATHOLIQUE DE LOUVAIN
École polytechnique de Louvain
Rue Archimède, 1 bte L6.11.01, 1348 Louvain-la-Neuve, Belgique | **www.uclouvain.be/epl**